Collective nature of high-Q resonances in finite-size photonic metastructures

Thanh Xuan Hoang,[1,*] Daniel Leykam,[2,†] Hong-Son Chu,[1] Ching Eng Png,[1]
Francisco J. García-Vidal,[1,3] and Yuri S. Kivshar[4,‡]

[1]*Institute of High Performance Computing (IHPC), Agency for Science, Technology and Research (A*STAR), 1 Fusionopolis Way, #16-16 Connexis, Singapore 138632, Republic of Singapore*
[2]*Science, Mathematics and Technology Cluster, Singapore University of Technology and Design, 8 Somapah Road, Singapore 487372, Republic of Singapore*
[3]*Departamento de Física Teórica de la Materia Condensada and Condensed Matter Physics Center (IFIMAC), Universidad Autónoma de Madrid, E-28049 Madrid, Spain*
[4]*Nonlinear Physics Centre, Research School of Physics, The Australian National University, Canberra ACT 2601, Australia*

(Received 4 May 2024; accepted 3 February 2025; published 26 March 2025)

We study high-quality factor (high Q) resonances in periodic and disordered arrays of Mie resonators from the perspectives of both Bloch wave theory and multiple scattering theory. We reveal that, unlike a common belief, the bound states in the continuum (BICs) derived by the Bloch-wave theory do not directly determine the resonance with the highest Q value in large but finite arrays. Higher Q factors appear to be associated with collective resonances formed by nominally guided modes below the light line associated with strong-coupling effect of both electric and magnetic multipoles. Our findings offer valuable insights into accessing the modes with higher Q resonances via bonding modes within finite metastructures. Our results underpin the pivotal significance of magnetic and electric multipoles in the design of resonant metadevices and nonlocal flat-band optics. Moreover, our demonstrations reveal that coupled arrays of high-Q microcavities do not inherently result in a stronger light-matter interaction when compared to coupled low-Q nanoresonators. This result emphasizes the critical importance of multiple light-scattering effects in cavity-based systems.

DOI: 10.1103/PhysRevResearch.7.013316

I. INTRODUCTION

High-quality factor Q nanophotonic resonances are important for various applications ranging from photonic crystal cavities for quantum photonics [1–3] to metasurfaces for ultrathin optical beam shaping elements [4–6]. The former are based on nominally infinite Q guided modes of photonic crystal slabs, while the latter employ finite Q Mie resonances of wavelength-scale particles. Remarkably, fine-tuning or special symmetries have been predicted to convert low-Q resonances into infinite-Q modes known as bound states in the continuum (BICs) [7,8]. While there has been enormous interest in the BIC concept, theoretical predictions regarding BICs as cavities with infinite Q diverge from practical implementations, with experimentally measured Q values limited to less than one million [9].

Both the photonic crystal cavity and the BIC approaches are inspired by analogies between matter and light waves. These concepts are rooted in the physics of scattering-free propagation observed in Bloch waves within infinite periodic photonic crystals [7,10]. Discrepancies between nominal and measured Q values are typically attributed to enhanced scattering losses arising from fabrication imperfections or finite sample sizes [9,11,12], which are both neglected in Bloch wave theory [7]. These discrepancies are exacerbated as the devices are scaled down, leading to much lower Q factors reported in nanophotonic systems compared to single microcavities, which support whispering-gallery modes with measurable Q in the billions [13]. Thus, while the BIC approach provides an elegant and intuitive way to understand the Q factors of Bloch waves, it lacks quantitative predictive power for real finite-size systems.

Here we study resonances supported by arrays of Mie-resonant nanoparticles from the viewpoint of multiple scattering theory (MST), schematically illustrated in Fig. 1. We show that the viewpoint of the scattering wave provides a simple way to understand the emergence of (quasi-)BICs and other high-Q resonances in metastructures and metasurfaces in terms of collective resonances whose Q scales with the size of the system, diverging in the limit of an infinite system. Intriguingly, our findings reveal that the collective resonances of coupled high-Q microcavities do not necessarily result in Q-factor divergence. This is in contrast to the pronounced divergence observed when coupling low-Q Mie resonators, highlighting the intricate physics involved in strong multiple-scattering effects. Our

*Contact author: hoangtx@ihpc.a-star.edu.eg
†Contact author: daniel.leykam@gmail.com
‡Contact author: yuri.kivshar@anu.edu.au

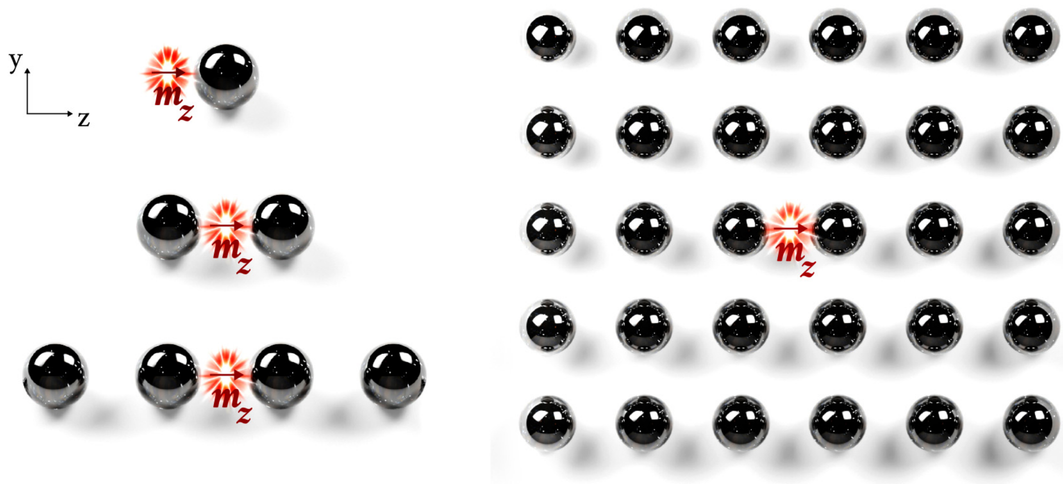

FIG. 1. Schematic of the interaction of a magnetic dipole with various structures: a meta-atom, a diatomic meta-molecule, a linear chain of spheres, and a two-dimensional (2D) array of spheres. Extending the chain and the 2D array to infinite periodic structures transitions them into photonic crystals capable of supporting Bloch waves, including bound states in the continuum.

findings not only provide conceptual clarity on the nature of high-Q resonances but also serve as a practical guide for designing resonant metastructures, starting from a single unit cell.

In the following, we will consider Mie-resonant silicon nanoparticles with a fixed sphere radius of 210 nm and a refractive index of 3.5. These parameters ensure that the high-Q collective resonances fall within the crucial near-infrared frequency range, essential for various technological applications [14,15], and are similar to recent experiments studying quasi-BICs [16–18].

II. BLOCH WAVES VS SCATTERING WAVES

In the weak-coupling regime, the emission rate γ of a light emitter interacting with its local three-dimensional (3D) electromagnetic environment is described by the multipolar interaction Hamiltonian:

$$H_{\text{int}} = -\boldsymbol{\mu} \cdot \mathbf{E}(\mathbf{r}_\mu, t) - \boldsymbol{m} \cdot \mathbf{B}(\mathbf{r}_m, t) - \dots . \tag{1}$$

Here $\boldsymbol{m}$ and $\mathbf{r}_m$ ($\boldsymbol{\mu}$ and $\mathbf{r}_\mu$) represent the magnetic (electric) dipole moment and position of the emitter, respectively. Equation (1) is applicable to investigate both the dynamical and stationary properties of the emission rate. Our focus lies on the stationary modes of BICs, where we employ predefined magnetic dipoles with constant moments across the entire frequency range of interest.

For systems involving magnetic dipole transitions at equilibrium, the emission rate is

$$\gamma = \frac{\omega}{2}\text{Im}\{\boldsymbol{m}^* \cdot \mathbf{B}(\mathbf{r}_m)\}. \tag{2}$$

In this context, ω represents the angular frequency associated with the dipolar transition. As our interest lies in the enhancement of γ due to emitter-environment interactions, we utilize the Purcell factor defined as:

$$F_P = \frac{\gamma}{\gamma_0}. \tag{3}$$

Here $\gamma_0 = c|\boldsymbol{m}|^2/(2h\omega)$, where c is the speed of light and h is Planck's constant, represents the emission rate of the emitter in the corresponding homogeneous material, which is vacuum in Fig. 1.

Equations (2) and (3) can effectively describe the interaction of a dipole with both Bloch waves and scattering waves, which correspond to different field profiles $\mathbf{B}(\mathbf{r}_m)$. The unique boundary conditions applied in solving Maxwell's equations for $\mathbf{B}(\mathbf{r}_m)$ result in significant distinctions between the two.

A. Bloch waves: Diffracted waves as open channels

For Bloch waves the electromagnetic field satisfies

$$\mathbf{B}(\mathbf{r} + \mathbf{R}_{nu}) = e^{i\mathbf{k}_B \cdot \mathbf{R}_{nu}}\mathbf{B}(\mathbf{r}), \tag{4}$$

where $\mathbf{R}_{nu}$ is the vector connecting the nth and uth unit cells. Numerical simulations are used to determine the magnetic field $\mathbf{B}(\mathbf{r})$ within the unit cell, using an excitation source at the temporal frequency f. For the linear chain in Fig. 1, Bloch boundary conditions are applied in the z direction, while perfectly matched layers simulate outgoing waves in the x and y directions. These outgoing waves propagate in vacuum with a wave number $k = 2\pi f/c$. The dispersion relation $k_B(f)$ is computed from these simulations.

When the Bloch wave number k_B is greater than the wave number k, the Bloch wave is classified as a guided mode [19], corresponding to a band located below the light line in the band diagram. Conversely, when k_B is less than k, the Bloch wave couples with a finite number of diffracted or open channels, which collectively form a continuum, characterized by their continuous spectra. The interaction with these open channels causes the bands above the light line to behave like leaky resonances, giving rise to the concept of guided resonances [20].

Later studies introduced the term "bound states" for guided bands, implying that Bloch waves, propagating without scattering, are truly bound with infinite Q factors. However, the finite nature of 1D or 2D photonic crystals inevitably leads to a complex interplay between Bloch waves and scattering waves [21]. These complexities are further amplified by recent developments in guided resonances, leading to the concept of Bloch BICs, which differ fundamentally from the original matter-based BICs [22–24]. Despite significant advancements, critical questions surrounding the physics of BICs remain actively debated [8,25].

Scattering effects, though inherently present, are often overlooked when studying light interactions with 1D or 2D photonic crystals. This work emphasizes that acknowledging these scattering effects, while recognizing the distinctions between light waves and matter waves, enables a unified understanding of BIC physics. Particularly, we show that achieving infinite Q factors does not necessarily require complete decoupling of light from the far-field region.

B. Scattering waves: Partial multipole and plane waves as open channels

The scattering field can be expanded using multipole and plane-wave representations as [26,27]

$$\begin{aligned}\mathbf{E}(\mathbf{r}) &= \sum_{l=1}^{L_{\max}} \sum_{m=-l}^{l} \left[\alpha_{lm}\mathbf{N}_{lm}^{(1)}(k\mathbf{r}) + \beta_{lm}\mathbf{M}_{lm}^{(1)}(k\mathbf{r})\right] \\ &= \frac{ik}{2\pi}\int_0^{2\pi} d\beta \int_{C^\pm} d\alpha \sin\alpha \hat{E}(\hat{s}) e^{i\boldsymbol{k}\cdot\boldsymbol{r}}, \end{aligned} \tag{5}$$

$$\begin{aligned}\mathbf{H}(\mathbf{r}) &= \sum_{l=1}^{L_{\max}} \sum_{m=-l}^{l} \left[\beta_{lm}\mathbf{N}_{lm}^{(1)}(k\mathbf{r}) - \alpha_{lm}\mathbf{M}_{lm}^{(1)}(k\mathbf{r})\right] \\ &= \frac{ik}{2\pi}\int_0^{2\pi} d\beta \int_{C^\pm} d\alpha \sin\alpha \hat{H}(\hat{s}) e^{i\boldsymbol{k}\cdot\boldsymbol{r}}. \end{aligned} \tag{6}$$

Here $\mathbf{N}_{lm}^{(1)}$ and $\mathbf{M}_{lm}^{(1)}$ represent electric and magnetic multipole fields behaving as outgoing waves at infinity, while α_{lm} and β_{lm} denote multipole expansion coefficients (MECs) specific to the interaction configuration. The spectral amplitude vectors $\hat{E}(\hat{s})$ and $\hat{H}(\hat{s})$ are related to the MECs, where $\hat{s}(\alpha,\beta) = \mathbf{k}/k$ is a unit vector with polar angle α containing real and complex values along the integration contours $C^\pm$. For convenience, we will use $\mathbf{H} = \mathbf{B}/\mu_0$ to refer to the magnetic field.

Complex values of α correspond to evanescent waves that decay exponentially in specific directions. Traditionally termed closed channels, these evanescent waves stand in contrast to their propagating counterparts, corresponding to the real values of α, known as open channels [16]. In the context of plane-wave expansion, emitters in Fig. 1 interact with both propagating and evanescent wave components. Despite far-field analysis typically overlooking evanescent waves, these emitters interact with both types, requiring energy dissipation into the far-field region to maintain equilibrium.

The stored energy within evanescent waves does not represent a true BIC; on deactivating the excitation source, the associated polarization energy gradually leaks into the far-field region. Moreover, individual plane waves, extending infinitely and implying infinite energy, are not physically realizable. In contrast, partial multipole fields offer a more comprehensible representation as physical waves.

Due to the positive energy of light waves, each multipole mode corresponds to a radiative, lossy oscillator. When resonant with a driving source, this oscillator behaves as a resonator that can achieve a high, though always finite, Q factor. These modes exist in 3D space and interact with multiple degrees of freedom, generating far-field patterns with intensities that vary in different directions, exhibiting maxima and minima based on their mode numbers. Crucially, all multipole modes remain open channels, continuously interacting with their 3D environment—an effect tied to the positive energy of light waves [28]. These characteristics are key to understanding the physics behind phenomena such as symmetry-protected and accidental BICs, as will be discussed later.

The importance of the far-field existence can be seen through the calculation of the system's time-averaged radiated power, derived from the multipole expansion detailed in Eqs. (5) and (6):

$$P = \frac{c}{8\pi}\sum_{l=1}^{L_{\max}}\sum_{m=-l}^{l} l(l+1)[|\alpha_{lm}|^2 + |\beta_{lm}|^2]. \tag{7}$$

An alternative approach to Eq. (3) involves computing the Purcell factor as $F_P = P/P_0$, where P_0 denotes the radiating power in the corresponding homogeneous environment. Equation (7) ensures the coexistence of both near- and far-fields.

Further insight into the energy carried by individual plane waves can be captured by Eq. (7). For example, considering a plane wave traveling in the z direction with circular polarization and an electric field $\mathbf{E} = (\hat{x} + i\hat{y})E_0 e^{ikz}$, the associated MECs are

$$\alpha_{l;1} = i\beta_{l;1} = \frac{E_0}{k} i^{l+1}\sqrt{\frac{\pi(2l+1)}{l(l+1)}}. \tag{8}$$

When expanded as a multipolar series of both incoming and outgoing waves [27], the power carried by such a plane wave can be evaluated from the outgoing multipole fields. In this context, combining Eqs. (7) and (8) yields $P = \frac{cE_0^2}{8k^2}\sum_{l=1}^{\infty}(2l+1)$, which is infinite and therefore unphysical. This highlights the limitations of plane-wave expansions in describing finite systems. Multipole modes, functioning as open channels, offer a more insightful framework for understanding light-matter interactions in metastructures.

III. COLLECTIVE ANTIBONDING AND BONDING PHOTONIC MODES

The theory of multiple Mie scattering allows us to express the field scattered by the uth sphere positioned at $\mathbf{r}_u$ in terms of a series of magnetic multipole fields $\mathbf{M}_{lm}^{(1)}$,

$$\mathbf{E}_u(\mathbf{r}_u) = \sum_{l=1}^{L_u} q_{l;0}^{(u)}\mathbf{M}_{l;0}^{(1)}(k[\mathbf{r}-\mathbf{r}_u]), \tag{9}$$

where the required truncation order L_u depends on the vacuum wave number k and the spheres' radius; here $L_u = 10$ is sufficient to obtain good agreement with a direct numerical solution of Maxwell's equations (Lumerical FDTD). Due to axial symmetry, the m_z source excites only the magnetic multipole modes with $m = 0$. The internal field of the uth sphere can be calculated in the MST in which we can relate its MECs $\eta_{l;0}^{(u)}$ to the MECs $q_{l;0}^{(u)}$ in Eq. (9) via $\eta_{l;0}^{(u)} = q_{l;0}^{(u)} d_l^{(u)}/b_l^{(u)}$, where $b_l^{(u)}$ and $d_l^{(u)}$ are the Mie coefficients.

Applying the MST results in the following equation, accounting for all short-range, long-range, and scattering couplings:

$$q_{l';0}^{(n)} = b_{l'}^{(n)} \left(A_{l';0}^{1;0}(\overrightarrow{OO_n})m_z + \sum_{u\neq n} \sum_{l=1}^{L_u} A_{l';0}^{l;0}(\overrightarrow{O_uO_n})q_{l;0}^{(u)} \right), \tag{10}$$

where $A_{l';0}^{l;0}(\overrightarrow{O_uO_n})$ translates the magnetic multipole field $\mathbf{M}_{l;0}^{(1)}$ from the uth sphere into the incident field approaching the nth sphere [29]. Equation (10) allows us to compute all the MECs to study the near- and far-field distributions, as well as the Purcell factor. The roles of Mie and translational coefficients in localizing light will be discussed later when we investigate the effects of introducing disorders into the sphere diameters and positions.

A. Intrinsic magnetic quadrupole and octupole modes in photonic meta-atoms

Because both photonic crystals and metastructures are composed of unit cells, it is useful to begin our investigation of high-Q resonances by discussing the intrinsic Mie modes of a single sphere. Additionally, as Q factors are a fundamental electrodynamic property, it is instructive to describe the formation of stationary Mie resonant modes within the framework of electrodynamics.

Figure 2 shows the multipolar analysis of the interaction between a magnetic dipolar emitter and a single sphere. In Fig. 2(b), the resonant wavelengths of the intrinsic magnetic quadrupole (MQ) and octupole (MO) modes are shown, with Q factors of 50 and 200, respectively. Generally, higher-order multipole modes exhibit higher Q factors, as observed here, due to the dominance of whispering-gallery modes in the light confinement mechanism of a single sphere. These modes rely on partial internal reflection, which progressively approaches total internal reflection for higher-order multipole modes.

Light circulates around the circumference of the sphere, experiencing multiple internal scattering events [30]. Only light with appropriate frequencies undergoes constructive interference, forming Mie resonant modes. In particular, these Mie modes are only established after a sufficient time of continuous excitation, their Q factor representing the time required to fully build up the resonance. In some cases, Q factors in the billions have been experimentally observed for sufficiently high-order modes.

However, while whispering gallery cavities achieve high Q factors, their bulkiness limits light manipulation at the nanoscale—a capability in which metastructures excel. The spectral distribution of F_P in Fig. 2(c) reveals peak wavelengths that align with the internal Mie coefficients, emphasizing that the Purcell enhancements are primarily driven by intrinsic modes. To validate the accuracy of the F_P calculations, we performed a numerical simulation using the FDTD software, with the result also shown in Fig. 2(c).

Typically, BICs and photonic crystal modes are analyzed on the basis of eigenmodes in individual unit cells. For subwavelength unit cells, only a few low-order Mie modes are necessary to describe these eigenmodes. We will next

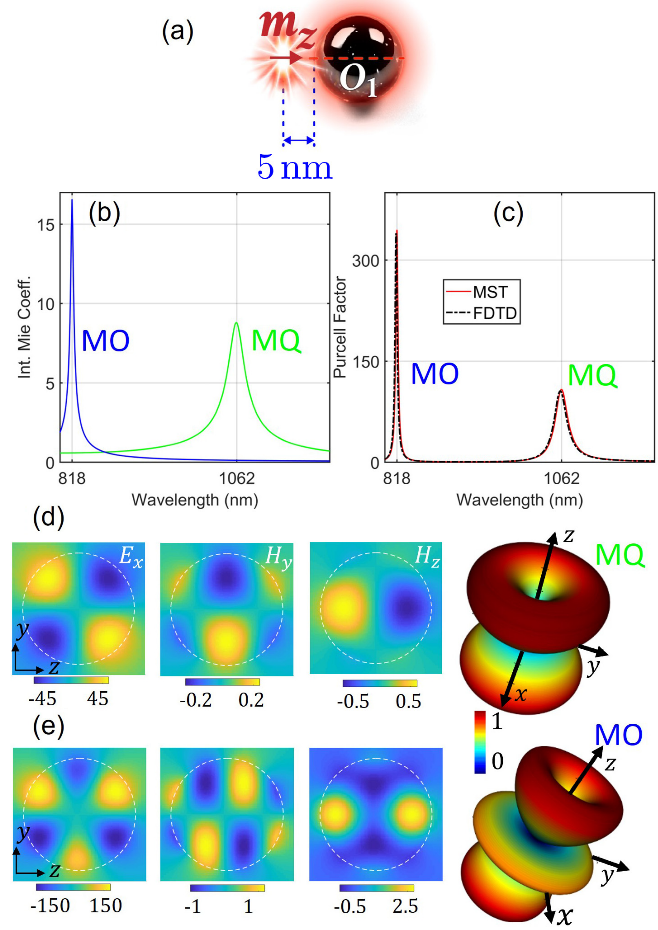

FIG. 2. (a) Schematic of a single magnetic dipole oriented along the z axis interacting with a single sphere. [(b) and (c)] Spectral profiles of the internal Mie coefficients and their corresponding Purcell factors: d_2 (MQ) and d_3 (MO). The MST result based on Eq. (7) closely matches the FDTD simulation using Eq. (3). [(d) and (e)] Near- and far-field patterns correspond to excitation of the MQ and MO peaks in (c). In the far-field region, the radiation patterns depend solely on the solid angle, and the magnitudes of the electric far-field distributions are normalized to the strongest radiation direction.

investigate the near- and far-field distributions of the MQ and MO Mie modes, which will facilitate subsequent discussions of BICs involving symmetry and interference arguments.

Figures 2(d) and 2(e) illustrate the near- and far-field distributions of the MQ and MO modes, respectively. Notably, the far-field distribution of the MQ mode in Fig. 2(d) exhibits a distinctive pattern, showing destructive interference in the transverse xy plane. This interference aligns with the antisymmetry of the MQ mode (particularly the E_x or H_z components with respect to the y axis), which has been used to support the presence of at-Γ BICs [31]. Another perspective for the existence of BICs is based on the symmetry of E_x relative to the center of the unit cell [7]. However, arguments based solely on individual electromagnetic components are insufficient. As we will discuss in greater detail later, understanding the destructive interference in the transverse xy plane and its connection to the near-field mode distributions requires

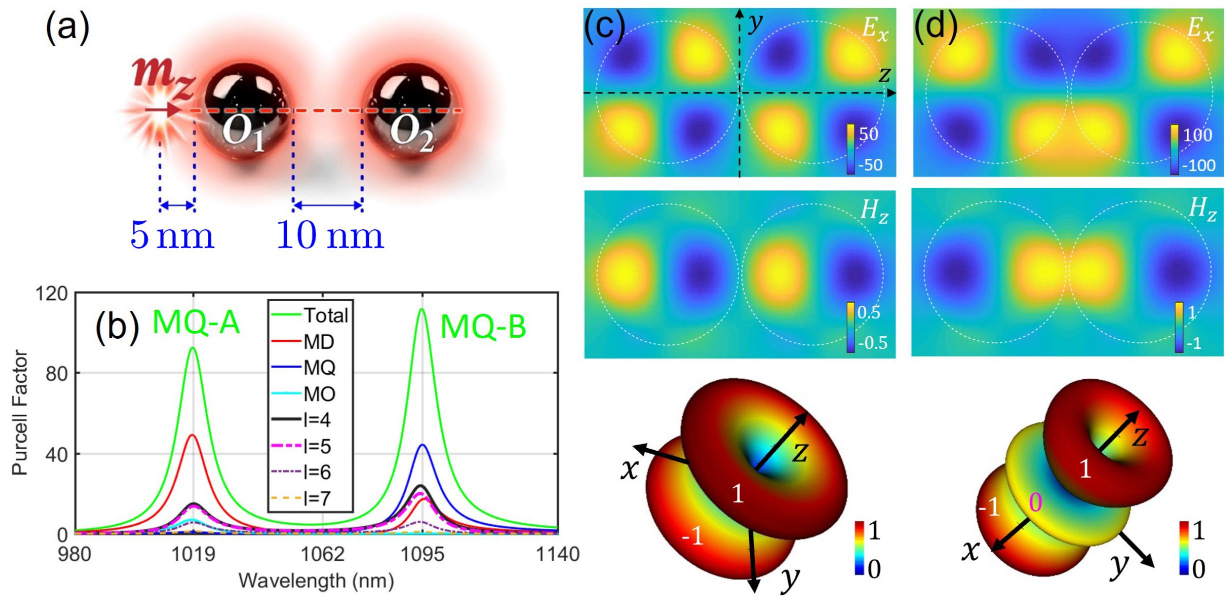

FIG. 3. (a) Schematic of the interaction between a z-oriented magnetic dipole and a diatomic photonic metamolecule. (b) Spectral profile of the total Purcell factor, showing splitting of the MQ mode into antibonding (MQ-A) and bonding (MQ-B) modes, corresponding to a magnetic null and a hotspot (H_z) at the center of the gap, as shown in (c) and (d), respectively. The multipole decomposition reveals that both modes exhibit contributions from the magnetic dipole ($l = 1$, MD), which radiates predominantly in the transverse xy plane. (c) Near- and far-field distributions of the MQ-A mode. The absence of the 0th scattering channel in the xy plane is caused by destructive interference between the magnetic dipole, the octupole, and a higher-order multipole ($l = 5$), which also leads to the antisymmetry of E_x with respect to the y axis. (d) Similar to (c) but for the MQ-B mode, where the 0th scattering channel appears due to the magnetic dipole and higher-order multipole ($l = 5$).

consideration of all three field components presented in Fig. 2(d). This discussion will clarify the symmetry mismatch mechanism responsible for Bloch BICs.

Another significant observation drawn from the far-field distributions in Figs. 2(d) and 2(e) is the absence of radiation in the z direction, which can be attributed to the vectorial characteristics of the longitudinal m_z dipole and its associated excited multipole modes. This vectorial nature has been used to explain the existence of at-Γ BICs [17,32], which are often confused with symmetry-protected BICs arising from diffraction theory [7]. We will show that at-Γ BICs and symmetry-protected BICs are distinct, and that the vectorial nature of a single unit cell cannot solely account for the existence of at-Γ BICs.

B. Antibonding and bonding magnetic quadrupole modes in diatomic metamolecules

The laws of electrodynamics dictate that modes of a dielectric structure, such as a meta-atom or a unit cell, must be radiatively lossy [28]. Consequently, coupling between these modes does not increase the total number of resonant modes (also referred to as closed channels) beyond the number of open channels. This principle holds even as the number of coupled resonators approaches infinity, implying the existence of an infinite number of open channels in MST. This behavior contrasts sharply with diffraction band theory, where interactions between plane waves and Bloch waves in infinite subwavelength periodic structures involve only a single diffraction channel [33] or a finite number of open channels [8]. Recognizing this fundamental difference between diffraction band theory and MST is essential for designing resonant metasurfaces, as practical devices are finite and thus require consideration of the infinite number of open channels. Moreover, understanding infinite periodic structures necessitates studying their finite counterparts and progressively increasing the system size. To address this, we will next investigate finite coupled meta-atoms, also referred to as metamolecules.

The simplest example of a coupled system is a diatomic metamolecule, schematically illustrated in Fig. 3(a). Figure 3(b) depicts the splitting of the intrinsic MQ mode into antibonding (MQ-A) and bonding (MQ-B) modes, driven by the strong optical coupling between the two meta-atoms. The peak wavelengths exhibit characteristic blue and red shifts for the antibonding and bonding modes, respectively, analogous to those observed in molecular physics. In this system, the antibonding and bonding features correspond to a magnetic H_z null and a hotspot at the gap between the two meta-atoms, as shown in Figs. 3(c) and 3(d).

Additionally, we decompose the total Purcell factor into contributions from partial multipoles, as represented by Eq. (7). Figure 3(b) shows that six multipoles are required to describe the intrinsic modes of the coupled resonators, with only the $l = 7$ multipole term being negligible across the spectral range. The collective MQ-A and MQ-B modes exhibit distinct multipole compositions that govern both their near- and far-field distributions through interference effects.

Point group theory is commonly used to explain symmetry-protected BICs, focusing primarily on the mode profiles of individual unit cells [32,34]. However, for later discussion, we note from Figs. 3(c) and 3(d) that, with respect to the center of the sphere, both the MQ-A and MQ-B modes exhibit the same symmetry in the E_x field distribution and antisymmetry in the H_z field distribution.

Point group theory alone cannot adequately explain the presence and absence of the 0th scattering channel in the far-field patterns of the MQ-A and MQ-B modes, respectively. Instead, we must consider the symmetry and antisymmetry of the collective modes about the y and z axes. Both near-field H_z distributions display symmetry with respect to the z axis; however, the E_x distribution of the MQ-A mode is antisymmetric, while that of the MQ-B mode is symmetric with respect to the y axis.

In the far-field region, light behaves as independent plane waves. To elucidate the absence and presence of the 0th scattering channel, we can consider a time-reversal process in which we excite the MQ-A and MQ-B modes using a plane wave incident along the x axis, with a magnetic field oriented along the z axis. Consequently, the electric component must align with the y axis according to the laws of electrodynamics. The antisymmetry of the E_x component with respect to the y axis in the MQ-A mode leads to a mismatch with the plane wave's electric component, preventing the plane wave from exciting the MQ-A mode. In contrast, the MQ-B mode matches the plane wave and is excited. This reversal argument explains the absence and presence of the 0th scattering channels in Figs. 3(c) and 3(d), corresponding to the destructive and constructive interference of odd-order magnetic multipoles ($l = 1, 3, 5$) shown in Fig. 3(b).

It is important to note that both the antisymmetry of the E_x component in the MQ-A mode and the absence of the 0th scattering channel in Fig. 3(c) result from the destructive interference of the multipole modes. In other words, attributing the absence of the 0th scattering channel in Fig. 3(c) to symmetry mismatch could be misleading in electrodynamics, as it may suggest that the MQ-A mode does not require the odd-order multipoles to represent its near- and far-field distributions [32].

IV. COLLECTIVE NATURE OF BOUND STATES IN THE CONTINUUM

This section investigates the physics underlying high-Q resonances in photonic crystals, framed through Bloch waves, and in metastructures through scattering waves, with focus on elucidating the mechanisms behind BICs. Photonic BICs have gained significant interest since they were first studied in infinite coupled gratings excited by plane waves [33], and especially after their observation in photonic crystal slabs [22]. Since then, the concept of BICs has attracted attention from both the photonic crystal and metamaterial communities [35].

Most studies focus on plane-wave excitations, where the disappearance of transmittance and reflectance at specific incident angles is attributed to BICs. When this disappearance occurs at normal incidence, the BICs are referred to as symmetry-protected and are commonly associated with the Γ point [7,36]. When the disappearance occurs at oblique incidences, these are labeled accidental BICs and are known as off-Γ BICs [22,31]. Symmetry mismatch and destructive interference have typically been invoked to explain the origins of symmetry-protected and accidental BICs, respectively.

Despite significant progress in both applications and fundamental studies of BICs, developing a unified physical mechanism for these states remains an open problem [8,25]. In this section, following Sec. III, we expand on the limitations of using symmetry arguments and destructive interference as explanatory frameworks. Our analysis reveals that collective resonances arising from strong multiple scattering provide a unified explanation for both high-Q and infinite-Q resonances. Furthermore, we show that symmetry-protected and accidental BICs are specific to plane-wave excitations and are not inherently equivalent to at-Γ and off-Γ BICs. These insights offer conceptual clarity to the various high-Q resonances observed in systems ranging from photonic crystals to metastructures, all of which are governed by multipolar scattering waves.

Our findings have practical implications for high-Q resonators in applications such as optical spectral filtering, sensing, and lasing. For spectral filtering or polarization conversion, BIC concepts are particularly valuable in designing metadevices based on coupled gratings or low-index-contrast photonic crystals. Although these systems weakly confine light in the in-plane directions and require larger physical footprints, making them less suitable for enhancing Purcell factors, they remain effective for targeted filtering and polarization conversion applications. In contrast, for applications requiring strong light-matter interactions, such as nanolaser development [16,17], where off-resonant pumping is typically employed, high-Q resonances corresponding to bound states below the light line result in devices with higher power efficiency [37].

A. At-Γ bound states in the continuum

Although both at-Γ BICs and symmetry-protected BICs can emerge in infinite periodic arrays, they represent fundamentally distinct phenomena. Symmetry-protected BICs arise when plane waves are incident on such arrays, typically exciting a set of Bloch modes, including the at-Γ Bloch mode. Even under normal incidence, the field in the periodic structure is a superposition of multiple Bloch waves. In contrast, at-Γ BICs correspond to single Bloch modes with a wave number of $k_B = 0$ and are generally excited by a dipole in the near-field region.

To further elucidate these key differences, we first examine at-Γ BICs excited by a magnetic dipole (see Fig. 4), followed by a discussion of off-Γ BICs in Sec. IV B. Symmetry-protected and accidental BICs are then analyzed in Sec. IV C.

1. Divergence and convergence of collective resonances

Figures 4(a) and 4(e) present two alternative perspectives on at-Γ BICs: one based on scattering waves and the other on Bloch waves. The key difference lies in the number of radiative channels: Scattering waves couple with an infinite number of plane-wave channels, whereas photonic crystals with subwavelength periods typically support only a single diffraction channel, which serves as the continuum channel for Bloch waves [33].

Figure 4(b) shows the emergence of two distinct bands from the MQ and MO modes as we transition from two spheres (Fig. 3) to 20, forming a 1D linear chain. These

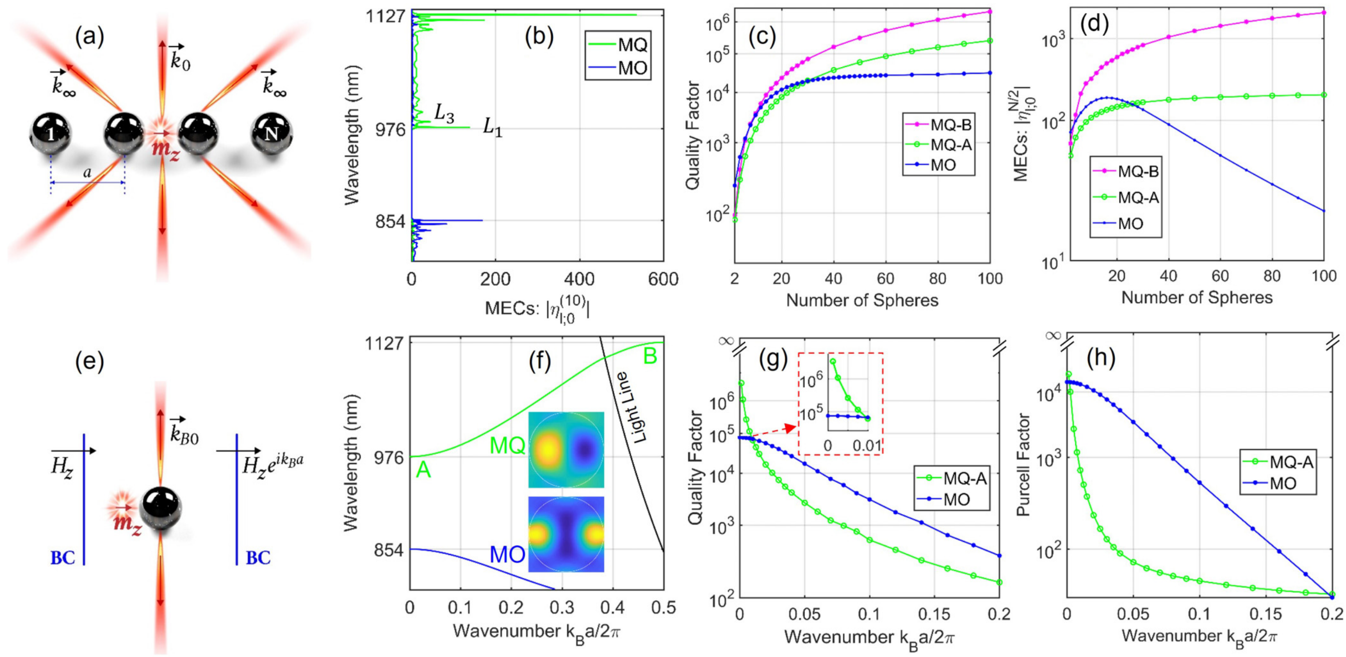

FIG. 4. Comparison of results from metastructure [(a)–(d)] and photonic crystal [(e)–(h)] analyses. (a) Schematic illustrating the interaction between a magnetic dipole and a metastructure composed of N spheres in a 3D environment with infinite degrees of freedom, represented by the wave vector $\hat{k}_\infty$. (b) Spectral profiles showing the MQ and MO expansion coefficients for a chain of 20 spheres, revealing two photonic bands with three prominent band-edge modes, corresponding to the MQ-A and MQ-B modes in Fig. 3 and the MO mode in Fig. 2. The MQ-A band-edge mode, labeled L_1, is stronger than the in-band collective modes, such as the L_3 mode. The collective mode L_2, which corresponds to a null field in the center of the array, does not appear in (b). (c) Q-factor analysis of the MQ and MO band-edge modes, highlighting their divergence and convergence as the number of spheres increases. (d) Divergence and convergence of the scattering multipole coefficients, representing the internal field localized in the middle sphere of the chain, as the number of spheres increases. (e) Schematic depicting the interaction between a magnetic dipole and a Bloch wave, with a single continuum diffraction channel denoted by the wave vector $\hat{k}_{B0}$. (f) Band diagram showing two photonic crystal bands corresponding to the MQ and MO bands in (b). The MQ band crosses the light line, while the MO band lies entirely above it. The insets show the antisymmetric and symmetric magnetic components H_z of the MQ and MO modes at the Γ point. (g) Q-factor analysis of the two Bloch modes above the light line, indicating a bound state in the continuum for the MQ-A mode at the Γ point. The inset magnifies the divergence and convergence near $k_B = 0$. (h) Purcell factor analysis showing divergence and convergence patterns consistent with the Q-factor analysis in (g).

collective bands suggest the existence of photonic crystal bands, a hypothesis confirmed by the Bloch band simulations in Fig. 4(f). Remarkably, the band edges in Fig. 4(f) closely match the predictions from the MST calculations in Fig. 4(b). Furthermore, the MST reveals collective resonances spread across the entire widths of the Bloch bands, both below and above the light line, highlighting the limited impact of the light line on resonator design using photonic metastructures. While collective resonances below the light line exhibit significantly higher strengths compared to those above it, their shared origin in resonant multiple scattering provides a unified perspective on guided resonances and Bloch bound modes.

Although the Q factors of the MQ-A and MQ-B modes are similar for two spheres, as shown in Fig. 3(b), their behaviors diverge significantly as the number of spheres increases, as seen in Fig. 4(c). In particular, the Q factor of the MQ bonding mode increases more rapidly than that of the antibonding mode. This divergence generally follows the power-law scaling described by $Q(N) \approx Q_0 N^\alpha$, where N represents the number of spheres. We estimate $\alpha \approx 3$ for the MQ-B modes, $\alpha \approx 2$ for the MQ-A mode, and $\alpha \approx 0$ for the MO mode.

The MQ-B mode, located below the light line, is conventionally described as a guided mode bound to the 1D photonic crystal, without extending into the far-field region. However, within the metacrystal MST framework, the MQ-B mode interacts with the far-field through scattering effects. While modes below the light line often exhibit much higher Purcell and Q factors, recent attention has shifted towards guided resonances above the light line, which promise infinite Q factors for enhancing light-matter interactions.

For infinite structures, the Q and Purcell factors associated with BICs can indeed reach infinity, as shown in Figs. 4(g) and 4(h) for the MQ-A and MO bands. As the Bloch wave number approaches the Γ point ($k_B = 0$), the Q factor of the guided MQ-A resonance diverges. Conventionally, this divergence has been attributed to the antisymmetric field component [31] [inset of Fig. 4(f)] or the symmetric E_x electric field component [7] (Fig. 2), both characteristic of the MQ mode. In contrast, the finite Q factor of the MO band arises from the symmetric component of the MO mode [inset of Fig. 4(f)] [31].

Challenges arise, however, when considering the symmetry properties of both the electric and magnetic field components of these modes. For an example, the field distribution of E_x

for both the MQ-A and MO modes is symmetric with respect to the center of the unit cell and the y and z axes, which means that symmetry alone cannot explain the divergence and convergence behavior shown in Fig. 4(g). Furthermore, as depicted in Fig. 4(a), our dipole excitation source primarily radiates in transverse directions, which contrasts with the behavior of an at-Γ BIC that does not radiate transversely. Another potential mechanism for the divergence of the Q factor in Fig. 4(g) and the Purcell factor in Fig. 4(h) is the destructive interference between the multipoles excited in the unit cell and the dipole driving source [22,32]. This wave interference mechanism is a fundamental property of wave physics and mirrors the explanation for the diatomic metamolecule system in Fig. 3.

However, to achieve complete destructive interference, the system would require infinite time to accumulate infinite energy within the unit cell, fully suppressing the transverse radiation of the source. Thus, while destructive interference is valid for stationary states, it does not fully apply to dynamic electrodynamic systems. In the FDTD results shown in Fig. 4(g), when we set the boundary conditions to isolate the Γ point the energy in the simulation domain does not decay to zero for the MQ-A mode but does for the MO mode. This behavior reflects the long-range effects present in coupled resonator systems [38]. The finite Q factor of the MO Bloch mode aligns with the converging Q factor obtained from MST, as shown in Fig. 4(c). This consistency between the MST and photonic crystal approaches is intriguing, especially considering their differing boundary conditions, but it is expected, since both derive from Maxwell's equations. Our view of BICs within the MST framework offers a consistent explanation for both finite and infinite systems, in both dynamic and stationary states.

In the MST the MQ mode, with its stronger long-range interactions, exhibits a strong (divergent) collective resonance, while the MO mode remains finite due to its weaker long-range interactions. Further insights into the impact of long-range interactions on the resonant MECs are elucidated in Fig. 4(d), illustrating the divergence and convergence of the MECs representing the resonant field inside the middle sphere. Due to the positive energy of light, adding more spheres to the chain introduces not only channels that enhance resonances but also radiative channels that weaken them. For both MQ-A and MQ-B modes, the enhancement effect outweighs the dissipative effect, resulting in the divergence of the MQ coefficients. In contrast, for the MO mode, the opposite occurs, leading to the convergence of the MO coefficient. These patterns of divergence and convergence in the resonant strengths elucidate the corresponding diverging and converging characteristics of the Purcell factors shown in Fig. 4(h), where we examine the interaction between the magnetic dipole and the Bloch MQ-A and MO modes.

Interestingly, high-Q Mie resonator (MO) arrays do not inherently produce higher collective resonance Q factors compared to arrays of low-Q Mie modes (MQs) with a sufficiently high number of resonators, as exemplified in Fig. 4(c). This peculiarity arises from the intricate interplay between the behavior of individual resonators and their collective response. Individual high-Q modes retain light for longer periods but also introduce heightened radiative-loss channels, limiting their collective resonances from reaching the strong multiple-scattering regime necessary for divergence. In fact, higher-order Mie modes behave similarly to whispering gallery modes, and coupling these high-Q modes generally results in collective Q factors lower than their isolated counterparts [29]. This finding can guide the design of coupled cavity arrays for applications such as quantum simulators and networks [39–41].

2. Near-field symmetry and far-field interference

Since symmetry mismatch and far-field destructive interference are two of the most common mechanisms for explaining BIC [8], it is instructive to investigate far-field interference patterns alongside the near-field symmetry and antisymmetry of the collective modes MQ-A and MQ-B, as shown in Fig. 5. The far-field patterns reveal destructive interference in multiple directions for both modes, which is not necessarily limited to the transverse direction. Moreover, it is crucial to recognize that the Bloch diffraction channel, characterized by the wave vector $\vec{k}_{B0}$, is distinct from the transverse radiation direction $\vec{k}_0$, as shown in Fig. 4(a).

Within the MST framework, even the MQ-B mode, corresponding to the bound state below the light line, radiates into the transverse direction, labeled the 0th scattering channel in Fig. 5(d). The presence and absence of this 0th scattering channel in Figs. 5(c) and 5(d), respectively, can be understood through the near-field distributions in Figs. 5(a) and 5(b). This reasoning follows a pattern similar to that in Sec. III for the diatomic metamolecule, where the symmetry and antisymmetry of the H_z and E_x distributions in the collective modes explain the behavior of the 0th scattering channel.

By extending this reasoning and increasing the number of unit cells to infinity, we observe that the absence of the 0th scattering channel persists for the MQ-A mode. In contrast, for the MQ-B mode, we can toggle the 0th scattering channel on or off by selecting an even or odd N, respectively, as the H_x distribution will exhibit symmetry or antisymmetry accordingly. For example, the 0th scattering channel disappears for $N = 1$ in Fig. 2(d) but reappears for $N = 2$ in Fig. 3(d) and $N = 20$ in Fig. 5(d). Therefore, we must consider the collective nature of resonant modes when examining their 0th scattering channel or its equivalent plane-wave excitation in a time-reversal process, as explained in Sec. III.

To further explore the far-field characteristics, we present the far-field intensity as a function of both excitation wavelength and polar angle in Fig. 5(e), focusing on the antibonding MQ-A mode [denoted L_1 in Fig. 4(b)]. A key distinction between the far-field plots in Figs. 5(c) and 5(e) is that the former shows the intensity at a single wavelength across the full polar angle range $(0, \pi)$ and half of the azimuthal angle range $(0, \pi)$, while the latter spans a range of excitation wavelengths and polar angles. Due to the system's axial symmetry, the far-field distributions are azimuthal invariant. The first scattering order from Fig. 5(c) and its associated L_1 wavelength are marked in Fig. 5(e) for clarity. Interestingly, the intensity along the transverse direction (90°) is not at a minimum, with several minimal points appearing at different angles and wavelengths. Some of these correspond to off-Γ points in Fig. 4(f), corresponding to guided resonances with

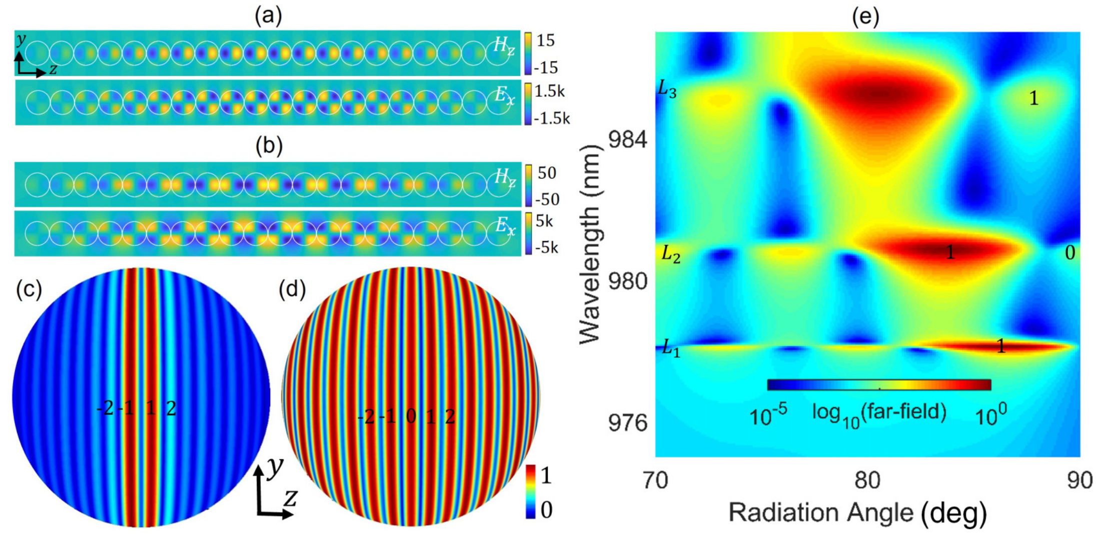

FIG. 5. Near-field symmetry and antisymmetry of bonding and antibonding modes and their corresponding multipolar interference in the far-field. [(a) and (b)] Near-field distributions of H_z and E_x for the antibonding MQ-A mode [L_1 in Fig. 4(b)] and the bonding MQ-B mode of a 20-sphere chain, respectively. The symmetry and antisymmetry of the field components align with the diatomic metamolecule presented in Fig. 3, leading to the absence of the 0th scattering channel in (c) for the MQ-A mode and its presence in (d) for the MQ-B mode. (e) Far-field intensity of antibonding modes as a function of the radiation wavelength and angle relative to the z axis. The collective Mie resonances L_1 and L_3 in Fig. 4 are marked at their respective peak wavelengths. For better visualization, the first scattering channel from (c) is also indicated in (e). The wavelength of the minimum intensity differs from the at-Γ BIC in Fig. 4, which occurs at 976 nm, highlighting the limitations of explaining BICs solely through destructive interference of multipoles or their symmetry properties.

finite Q factors. As such, the attribution of BIC formation solely to far-field destructive interference of multipole modes is not universally conclusive.

Another noteworthy feature in Fig. 5(e) is that, unlike the modes labeled with odd numbers (L_1 and L_3), the mode labeled L_2 produces the 0th scattering channel. This observation is significant because it indicates that the L_2 mode can be excited by a plane wave incident from the transverse direction. As we increase N, the mode L_2 will converge to the mode L_1, exhibiting an infinite Q. This further emphasizes the importance of considering the collective nature of the resonant modes when explaining their radiation into the 0th scattering channel. The role of plane-wave excitations in the formation of BICs will be discussed in further detail in Sec. IV C.

3. Material absorption limits on Q factor saturation

The Q-factor divergences in Fig. 4 pertain to chains of lossless silicon spheres. Recent studies have increasingly focused on the fundamental limits of Q factors due to material absorption losses [42]. Generally, the total Q factor is determined by both radiative (Q_r) and absorptive (Q_{abs}) components. For a material with permittivity $\epsilon' + i\epsilon''$, the absorptive Q factor is given by $Q_{\text{abs}} = \epsilon'/\epsilon''$.

In Fig. 6, we explore the Q-factor behavior of the MQ-A and MQ-B modes for lossy silicon, with a refractive index of $3.5 + i \times 10^{-4}$, corresponding to $Q_{\text{abs}} = 1.75 \times 10^4$. Unlike the rapid divergence of Q factors seen in the lossless case, Fig. 6(a) shows that in the presence of absorption, the Q factors converge to approximately Q_{abs}, highlighting the significant impact of material absorption. The fact that the saturated Q factors exceed Q_{abs} can be attributed to an effective scaling factor, which suggests that the saturated Q factor depends on the fraction of electromagnetic energy stored within the spheres [43].

Figure 6(b) reveals an intriguing result: the maximum Q factor of Bloch modes exceeds Q_{abs} by an order of magnitude and differs from the MQ-B band-edge mode predicted by the MST. Instead, this maximum corresponds to a Bloch mode near the light line. This discrepancy arises from the stronger confinement of the MQ-B band-edge mode to the spheres, which increases the absorption losses. However, for finite chains, the MQ-B band-edge mode consistently exhibits the highest Q factor, underscoring the importance of accounting for finite-size effects in light-matter interaction systems.

BICs are typically regarded as radiationless modes, where $Q_r \to \infty$, implying that the total factor Q is governed solely by material absorption, which is equivalent to Q_{abs},

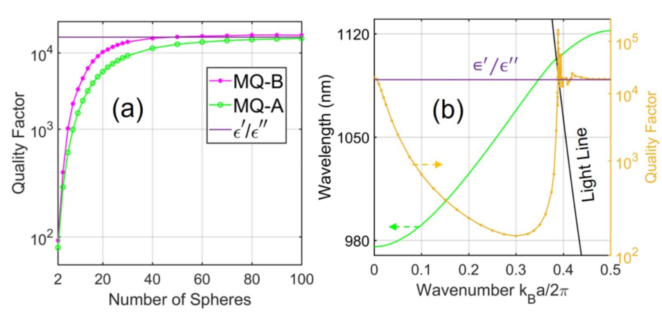

FIG. 6. Effect of material absorption loss. (a) Both bonding and antibonding MQ modes exhibit Q factors converging to values limited by absorption loss. (b) The convergence of Q factors for the two band edge Bloch modes corroborates findings from multiple scattering theory in (a).

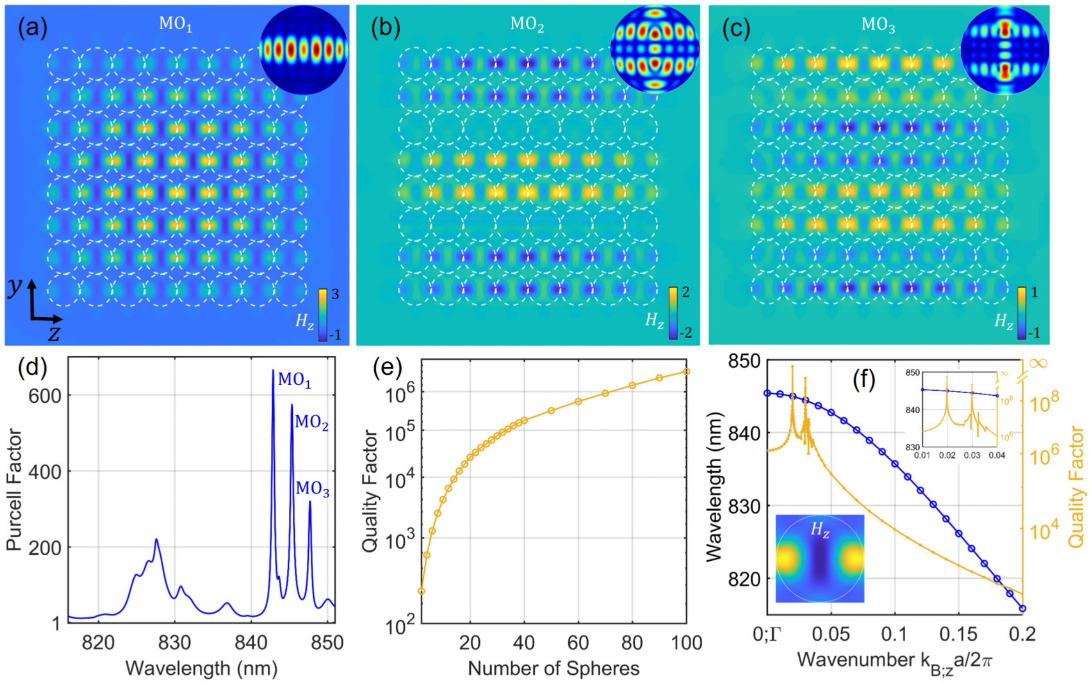

FIG. 7. Off-Γ bound states in the continuum arising from collective MO resonances in square arrays of $N \times N$ spheres. [(a)–(c)] Near-field H_z distributions for a 8×8 sphere array, corresponding to the $MO_{1,2,3}$ modes marked in (d). Insets show the respective electric far-field distributions. (d) Purcell factor for a z-oriented magnetic dipole placed at the location of the strongest field in (a). (e) Divergence of the Q factor for the MO_1 mode as the number of spheres in the square array (N) increases. (f) Band structure and divergence of the Q factor at off-Γ points, indicating the presence of BICs. The upper inset zooms in on the strong fluctuations of the Q factor near the BICs, while the lower inset shows the magnetic profile of the corresponding eigenmode.

according to the relation $1/Q = 1/Q_r + 1/Q_{\text{abs}}$ [42]. However, our MST framework provides an alternative explanation for the observed convergence of the Q factor. In this framework, radiation loss persists (finite Q_r), but long-range coupling effects weaken, preventing the divergence of partial multipole fields as the number of unit cells increases. It should be noted that the Q factors in Fig. 6(a) are derived from multipole scattering coefficients, indicating that saturation of the Q factor does not imply the absence of radiation loss.

B. Off-Γ bound states in the continuum

This subsection addresses the collective resonance origin of off-Γ BICs. As shown in Sec. IV A, the at-Γ BIC corresponds to the divergence of resonant scattering multipole fields. In contrast, the Q-factor convergence of the MO mode in the 1D photonic crystal results from radiative losses outweighing resonant enhancement, which is driven by long-range coupling effects. A practical approach to mitigate this radiative loss is to extend the structure into a 2D array or metasurface, as illustrated in Fig. 7. By transforming the 1D chain into the 2D metastructure, the light leaking into the y direction is redirected towards the central region, thus improving light-trapping efficiency.

Resonant metasurfaces typically support multiple supermodes [34,44,45], exemplified by $MO_{1,2,3}$ in Figs. 7(a)–7(d). The near-field H_z distributions of these supermodes clearly reveal their collective nature. The far-field distributions, shown in the insets of Figs. 7(a)–7(c), display several null-field directions, a characteristic feature of collective resonances. Notably, the dominant MO_1 supermode deviates from the band-edge behavior observed in its 1D chain counterpart (Fig. 4). This suggests that within the photonic crystal framework, the maximum factor Q of the corresponding guided resonance occurs at an off-Γ point rather than at Γ.

Furthermore, Fig. 7(e) illustrates the divergence of the Q factor for the MO_1 supermode as the number of spheres in the square metastructure increases. This divergence indicates that BICs could potentially be observed in the corresponding 2D photonic crystals, with the Q-factor divergence of collective resonances serving as a mechanism to detect BICs. Simulations of the photonic crystal band and its associated Q factors, shown in Fig. 7(f), support these hypotheses. The lower inset of Fig. 7(f) shows the H_z distribution within a unit cell, which remains nearly uniform across the entire band, while the upper inset reveals strong fluctuations of the Q factor near the BIC points, a typical signature of destructive and constructive interference between the Bloch and radiation modes.

Our findings provide important insights: While the theoretical Q factors of BICs tend toward infinity, experimental results typically achieve values below one million [9]. As shown in Fig. 7(e), even for a 100×100 resonator array, the Q factor reaches only around 1 million. Notably, a BIC laser with a factor Q in the thousands has been realized using a 16×16 MO array [16], consistent with our simulation in Fig. 7(e). Comparing these results with the 1D arrays in Fig. 4(c), it is evident that 2D MQ arrays can significantly enhance the efficiency of MO-based surface-emitting lasers. In Sec. IV D, we will show that these 2D MQ arrays can improve the Purcell factor by orders of magnitude.

The MO-based BIC has been linked to Friedrich-Wintgen BICs, which arise from coupled resonances [16,35]. However, Friedrich-Wintgen BICs require a critical condition: The number of closed channels must exceed that of the continuum channels [7], which light waves do not obey. A more appropriate term to describe BICs originating from coupled resonators could be Feshbach-type BICs, based on Feshbach's unified theory of coupled resonances interacting with multiple open channels [14]. Given the similarities between Feshbach's theory and our MST approach, it provides a better framework for explaining off-Γ BICs.

Past efforts to explore the impact of finite-size effects on off-Γ BICs relied on the tight-binding model for Bloch waves, attributing scattering loss primarily to the edges of finite structures [43,46]. However, our MST offers a contrasting perspective, revealing that the scattering loss predominantly originates from central regions [38]. These differing perspectives stem from the analogous yet distinct behaviors between matter and light waves. The concept of Bloch waves, rooted in matter waves traversing crystal lattices without scattering, hinges on two fundamental properties. First, matter waves and their potential structures can be considered closed systems if their total energy is negative, which limits the interaction between the matter waves and their environment. Second, when these matter waves interact with their local lattice potentials, they do not encounter retardation effects due to their probabilistic nature [47].

Conversely, light waves possess positive energies, and thus the internal fields within the unit cells of metacrystals—or metastructures in general—maintain coupling with the 3D environment even when we extend their structure to infinity. Moreover, in scenarios of resonant multiple scattering, light waves experience retardation effects, a crucial consideration. Unlike matter waves, the localization of light in resonant metacrystals does not rely on structural disorders, which are required for localizing matter waves through the Anderson effect. Essentially, the central localization of light within the resonant metasurface, as depicted in Fig. 7(a), and its associated van Hove singularity at the off-Γ points stem from the distinctive retardation effects inherent to light waves. Our findings elucidate these distinct attributes of photonic BICs, providing clarity on their physical origin.

C. Symmetry-protected and accidental BICs

The majority of BICs have been discussed in the context of the disappearance of reflectance and transmittance for plane waves incident on photonic crystal slabs or metasurfaces with subwavelength unit cells. Typically, BICs are classified into symmetry-protected (S-BIC) and accidental (A-BIC) types [35], corresponding to plane waves with normal and oblique incidence, respectively. These S-BICs and A-BICs are also commonly referred to as at-Γ and off-Γ BICs [7,22,23,36]. However, in Fig. 8, we present an alternative perspective. Although the disappearance of reflectance and transmittance is linked to resonant Mie modes in infinite metastructures, S-BICs and A-BICs do not necessarily align with the classifications of at-Γ and off-Γ BICs.

1. Disappearance of diffraction bands under oblique incidences and plane-wave coupling to Bloch modes

Figure 8(a) shows a typical setup for detecting BICs, where a plane wave with an incident angle θ interacts with a metasurface composed of subwavelength unit cells. According to diffraction theory, only a single diffraction channel governs the interaction between the plane wave and the metasurface, the reflectance following the law of specular reflection [48]. In this work, we employ rigorous coupled-wave analysis (RCWA) to compute transmittance and reflectance.

Figures 8(b) and 8(c) illustrate the transmittance for both S-polarized (T_s) and P-polarized (T_p) plane waves across a spectral range designed to detect the A-BIC, which shares its MO origin with the off-Γ BICs presented in Fig. 7. Six diffraction bands are identified within these parameter ranges, labeled B_{1-6} in Figs. 8(b) and 8(c). Notably, the A-BIC is observed in band B_2 at a wavelength of 865 nm and an incident angle of approximately 10°. This wavelength is 20 nm away from the off-Γ BIC, which appears at around 845 nm in Fig. 7(f). The 20-nm difference emphasizes that while the A-BIC and the off-Γ BIC originate from a common MO resonance, they represent distinct phenomena. This MO origin is further supported by the $E_\perp$ distribution within the unit cell, as shown in the inset of Fig. 8(b).

Additionally, the bands B_2 and B_4 are doubly degenerate at normal incidence ($\theta = 0^\circ$) and couple with a normally incident plane wave, consistent with a previous observation [36]. This degeneracy is confirmed by the convergence of the two bands as $\theta \to 0^\circ$ and the corresponding field distributions in the insets of Figs. 8(b) and 8(c). Although it is commonly believed that normal incidence interacts only with the at-Γ Bloch wave [7], Fig. 8(d) demonstrates that a normally incident plane wave actually couples with multiple Bloch waves representing the eigenmode. Our RCWA simulations include 60 Bloch modes to capture the eigenmode field, even at $\theta = 0^\circ$.

To further illustrate the significance of including all these 60 Bloch modes, we conducted an FDTD simulation considering only the at-Γ Bloch mode. The results in Fig. 8(d) reveal a peak wavelength shift from 876 to 802 nm. This 802-nm wavelength also differs from the at-Γ Bloch mode presented in Fig. 7. The discrepancy stems from the fundamental difference between plane wave and dipole excitations. A plane wave simultaneously excites various partial multipoles, driving the unit cell nonlocally through interactions with neighboring cells. In contrast, a dipole source excites the unit cell locally, with intercell interactions accounted for by applying Bloch boundary conditions.

2. Vanishing diffraction bands under normal incidence

Next, we focus on the physics behind S-BICs. Although four S-BICs are associated with the bands B_1, B_3, B_5, and B_6, the underlying diffraction theory explaining the disappearance of transmittance and reflectance is consistent across all. Therefore, we will focus on the S-BIC related to the band B_3. The $H_\perp$ and $E_\parallel$ field distributions shown in the insets of Fig. 8(d) reveal that this S-BIC arises from the antibonding mode of electric quadrupoles (EQs). Hence the in-plane electric field

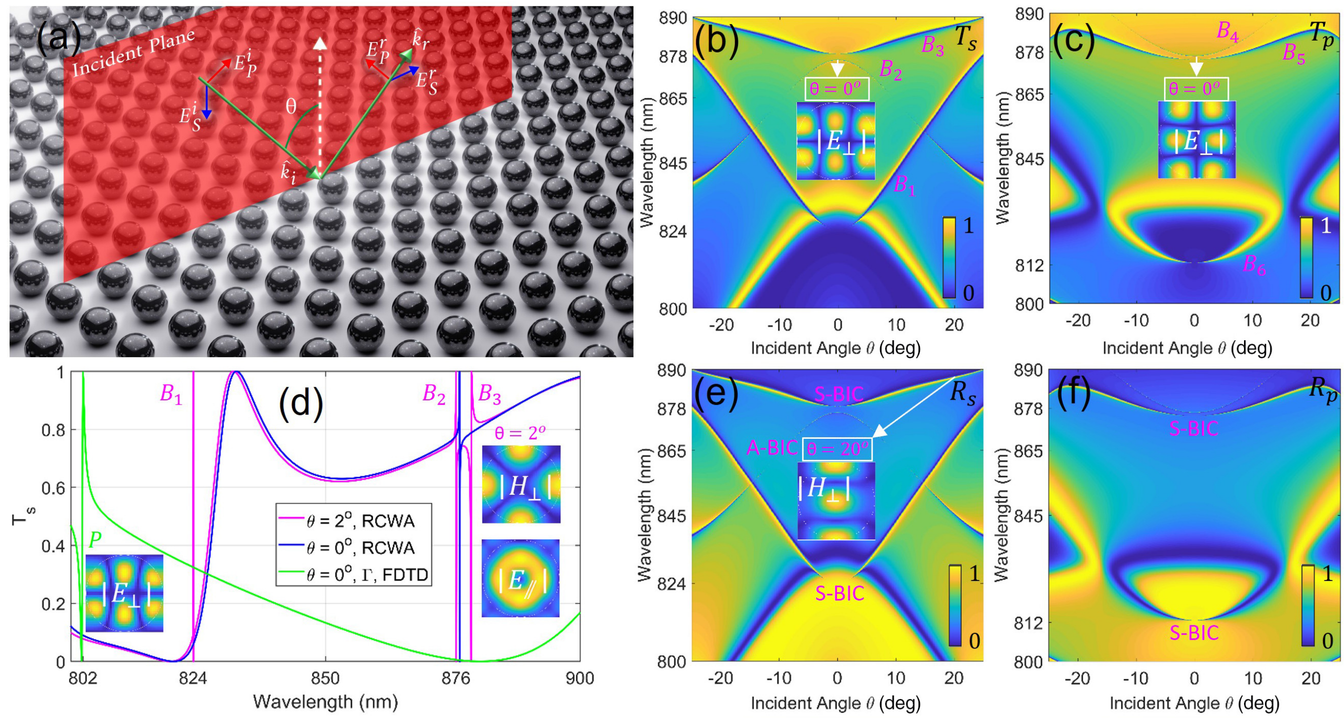

FIG. 8. Analysis of symmetry-protected (S-BIC) and accidental (A-BIC) bound states in the continuum via diffraction bands, arising from the interaction between an incident plane wave and a metasurface supporting Bloch waves. (a) Schematic of a conventional S-polarized (E_S^i) or P-polarized (E_P^i) plane wave incident on a metasurface formed by a square lattice of the spheres, leading to reflected S-polarized (E_S^r) and P-polarized (E_P^r) waves. (b) Transmission bands for the S-polarized wave, showing three bands (B_1, B_2, B_3) where BICs occur. Bands B_1 and B_3 vanish as $\theta \to 0^\circ$, indicating two S-BICs, while B_2 disappears near $\theta = 10^\circ$, marking an A-BIC. (c) Transmission bands (T_p) for the P-polarized wave, displaying bands B_4, B_5, and B_6. Band B_4 is doubly degenerate with B_2, as seen by their converging wavelengths at $\theta \to 0^\circ$ and the corresponding near-field distributions in the insets. Bands B_5 and B_6 disappear at $\theta = 0^\circ$, indicating two S-BICs. (d) Transmission spectra for the S-polarized wave at incident angles $\theta = 2^\circ$ and $\theta = 0^\circ$, highlighting the disappearance of the transmittance (T_s) associated with bands B_1 and B_3 at $\theta = 0^\circ$. FDTD simulations of the transmittance profile at the Γ point are included. Insets near the peaks show mode profiles, with the $|H_\perp|$ profile for B_3 at $\theta = 2^\circ$ differing significantly from $\theta = 20^\circ$ [inset in (e)], attributed to plane-wave excitation. The electric mode profile ($E_\parallel$) reveals null fields in the gap between unit cells, confirming the antibonding nature of B_3. [(e) and (f)] Reflection bands (R_s and R_P) corresponding to the transmission bands in (b) and (c), illustrating the relationship $T_{s,p} + R_{s,p} = 1$.

is localized inside the sphere, with null fields at the center gap between neighboring unit cells.

It is noteworthy that the near-field distribution of band B_3 changes significantly with the incident angle θ, see for example the difference between the $H_\perp$ distribution at $\theta = 2^\circ$ in Fig. 8(d) compared to that at $\theta = 20^\circ$ in Fig. 8(e). This variation arises from the plane-wave excitation, which drives multiple multipole modes simultaneously and nonlocally across the entire metasurface. As θ approaches 0°, the EQ mode dominates the interaction, and the near-field distribution shows the characteristic EQ pattern at $\theta = 2^\circ$. This contrasts with the local dipole excitation, such as in Fig. 4, where the near-field distributions remain relatively unchanged throughout the bands. A significant shift for the MQ band occurs near the light line, where the band transitions from an antibonding to a bonding mode.

Additionally, certain regions in Figs. 8(b), 8(c), 8(e), and 8(f) correspond to total reflection and transmission ($R_{s,p}, T_{s,p} = 1$). In these regions, multiple Mie modes, excited by the incident plane wave, contribute to the response. The phases of these intrinsic Mie modes cover a broad spectral range. Since no single Mie mode dominates, the diffraction bands remain spectrally broad, reflecting the weakly oscillating and phase-dispersed nature of the collective Mie mode interactions.

The disappearance of band B_3 at $\theta = 0^\circ$ raises a fundamental question: Does the S-BIC represent a resonance with an infinite Q factor and strong electromagnetic enhancement, or does it indicate that no resonance is excited at all? This issue is nontrivial because, in practice, metastructures are finite, and the S-BIC typically becomes a quasi-BIC that couples to the far-field region. If the S-BIC corresponds to a resonance with an infinite Q factor, then its quasi-BIC counterpart would couple efficiently with a normally incident plane wave. Conversely, if the S-BIC signifies that no resonance is excited, then the quasi-BIC may not couple efficiently with the plane wave. To resolve this ambiguity, we illustrate the coupling between a finite array of 8×8 spheres and both a plane-wave and a dipole source in Fig. 9.

3. Excitation dynamics of antibonding modes

Figures 9(a) and 9(b) present the results for normally incident plane-wave and x-oriented dipole excitations, respectively. The plane wave has its electric and magnetic field components aligned along the y and z axes. For the

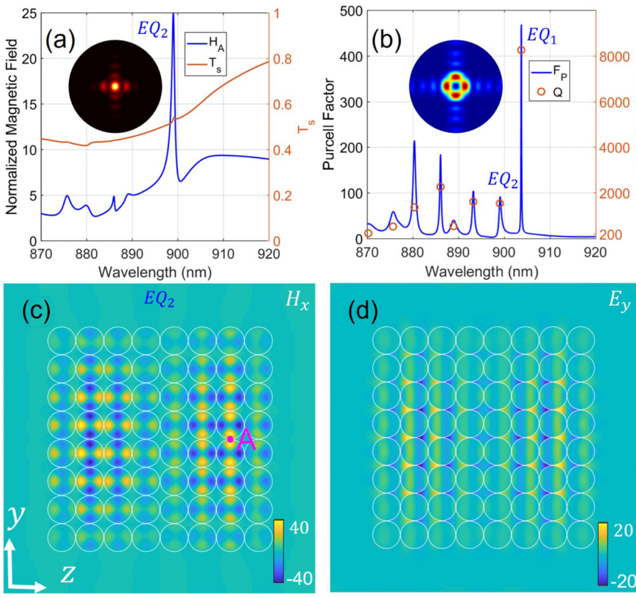

FIG. 9. Far- and near-field excitations of antibonding collective resonances associated with the S-BIC from band B_3. (a) Spectral profile of the magnetic field, normalized to the incident plane wave at $\theta = 0^\circ$, recorded at the gap center between two spheres in an 8×8 array [point A in (c)]. Even magnetic modes (EQ_2) are observed, while odd modes like EQ_1 are not excited. The transmittance (right axis) shows weak coupling to the plane wave, with only a 1% change at the resonant peak. The inset shows the far-field distribution of transmitted light at the EQ_2 peak, normalized to the strongest direction at $\theta = 0^\circ$. (b) Spectral profile of the Purcell factor for an x-oriented magnetic dipole at the point A in (c), with the corresponding Q factor (right axis). Both odd and even modes are excited by the dipole. The inset shows a vortexlike far-field distribution for EQ_1. [(c) and (d)] Near-field distributions of H_x and E_y at the EQ_2 peak, showing symmetry with respect to the z and y axes, respectively, with H_x originating from the electric quadrupole resonance associated with the S-BIC.

transmittance T_s evaluation shown in Fig. 9(a), a total-field scattered-field source is employed. This configuration ensures that only the array area is illuminated, allowing for accurate calculation of transmittance for the finite lattice. This plane wave excites only the even mode, specifically the EQ_2 mode, as shown in Fig. 9(a), with corresponding near-field distributions of H_x and E_y displayed in Figs. 9(c) and 9(d). The stronger EQ_1 mode is not excited because its E_y distribution is antisymmetric with respect to the y axis, leading to a mismatch with the electric field of the incident plane wave. This is similar to the behavior observed in Fig. 5(e), where the even collective mode L_2, analogous to the EQ_2 mode, radiates orthogonally to the array axis, and can be excited by a plane wave through a time-reversal process. In contrast, the B_3 S-BIC in Fig. 8 corresponds to a band edge mode [EQ_1, analogous to the collective mode L_1 in Fig. 5(e)] with an E_y distribution that is antisymmetric with respect to the y axis, preventing coupling with the plane wave. This suggests that the S-BIC does not represent a resonance with an infinite Q factor, instead no resonance is excited.

Although symmetry allows coupling between the even mode EQ_2 and the plane wave, this coupling is relatively weak, as shown by the spectral transmittance plot in Fig. 9(a), where the transmittance changes by only 1% at the resonant peak. The inset of Fig. 9(a) reveals that the 0th diffraction order does not vanish but instead dominates the far-field distribution of the transmitted light. If we extend the square lattice to infinity, then the collective EQ_2 mode will approach the behavior of the EQ_1 mode. This is because the EQ_2 mode can be viewed as two weakly coupled resonators separated by the y axis, and in the infinite limit ($N \to \infty$), these two modes, comprising $N \times (N/2)$ spheres, will converge into the EQ_1 mode, where $N \times N$ spheres resonate in unison. In other words, the vanishing of the 0th diffraction order is not a requirement for explaining collective resonances in Mie-tronics, even for modes with infinite-Q factors. Additionally, the presence of higher diffraction orders is noteworthy, as it may offer advantages for nonlocal flat optics.

The collective resonances in all-dielectric metastructures driven by plane waves are analogous to surface lattice resonances observed in arrays of plasmonic particles [49,50]. This similarity arises because both plasmonic and dielectric particles function as lossy oscillators capable of trapping light and enabling coupling effects. While collective resonances in plasmonic and dielectric metastructures may differ in quantitative analyses, their qualitative behaviors remain similar [51]. The modes EQ_1 and EQ_2 are typically referred to as dark and bright modes, respectively. In this context, a dark mode, such as EQ_1, indicates that it does not couple with a specific plane wave [52]. However, this does not imply complete decoupling from the far field if the mode is excited by a quantum emitter in the near-field region.

The far-field decoupling phenomenon relates to the definition of BICs based on a specific plane wave, as proposed in Ref. [7]. The confusion arising from this definition is that all plasmonic dark modes, including the EQ_1 mode, could technically be classified as BICs, even though they possess finite Q factors, as exemplified by the EQ_1 mode in Fig. 9(b). This introduces a contradiction: A resonance with a finite Q is categorized as having an infinite Q. Clarifying this ambiguity in the definition of BICs is nontrivial, as it directly impacts strategies for optimizing Purcell enhancements for emitters interacting with the collective resonances of finite-size metasurfaces.

Unlike plane-wave excitation in diffraction theory, a dipole can excite both odd and even modes, as demonstrated in Fig. 9(b). In this scenario, all collective modes are classified as bright modes. The brightness of these modes is quantifiable through the spectral profile of the associated Purcell factor in Fig. 9(b), which also presents the Q factors of the bright collective modes. The strongest resonance, EQ_1, produces a vortex-like far-field pattern, a key feature associated with BICs [23]. Notably, this far-field pattern differs significantly from the transmitted pattern shown in Fig. 9(a). In other words, the topological property of the EQ_1 mode refers to the intrinsic mode excited by the dipole. In addition, while plane-wave excitation can detect collective resonances, it does not provide evidence of infinite Q resonances.

In the framework of diffraction theory, our system shares the same underlying physics as periodic high-contrast gratings [53]. Photonic BICs were first introduced in optics through optically coupled gratings and have since found a wide range of applications, including those in polaritonics and optical trapping [54,55]. Although coupled gratings have been proposed as stand-alone high-Q resonators to enhance light-matter interactions, such as in compact laser development [53], their practical implementation often involves integration with additional reflectors [56], where coupled gratings function as efficient reflectors, much like metasurface reflectors [57].

One limitation of coupled gratings in trapping light from emitters, such as quantum dots, is their waveguide-like behavior along the grating axes, which directs light emission away from the source. As a result, the Purcell factors of coupled gratings are lower compared to those produced by the collective resonances of Mie modes. However, under plane-wave excitation, coupled gratings can still resonantly trap light through their supermodes [53]. This resonant effect, along with its associated BICs, is peculiar to the interaction between plane-wave excitation and coupled gratings. It occurs when the incident plane wave is aligned orthogonally to the grating axes, thereby preventing light propagation along the grating direction. This observation not only helps to distinguish between near- and far-field excitation schemes but also informs our design strategy for enhancing Purcell factors in Mie-tronics. In the next subsection, we will show thar bonding modes are better for boosting Q and Purcell factors than their antibonding counterparts.

D. Superiority of bonding modes in Mietronics

In this subsection, we discuss the implications of our findings for light localization in Mie-tronics, emphasizing that bonding collective resonances are typically orders of magnitude stronger than their antibonding counterparts. We also demonstrate the robustness of collective resonances against moderate levels of disorder.

1. Effects of weak disorder on collective resonances

We have established that for 1D metastructures, bonding modes corresponding to bound states in photonic crystals outperform their antibonding counterparts, which correspond to guided resonances, in providing both Q and Purcell enhancements. However, the most commonly studied metastructures are 2D arrays. Therefore, it is important to investigate bonding modes in metasurfaces under dipole and plane-wave excitations and to contrast them with the antibonding modes discussed above. These investigations will uncover their key advantages for relevant applications. Figure 10 illustrates that bonding collective resonances provide improvements of two orders of magnitude in both Purcell and Q factors compared to antibonding resonant modes, as demonstrated through the MO and EQ modes presented in Figs. 7 and 9.

The Purcell and Q factors resulting from the interaction of a z-oriented magnetic dipole, positioned at the gap center between two middle spheres within the 8×8 sphere array, are shown in Fig. 10(a). To further study the influence of fabrication-induced diameter variations, we generate five samples in which the diameters of the spheres are given by $D = D_0 + \sigma_D U_D$, where $D_0 = 420$ nm, σ_D is the degree of disorder, and U_D is a pseudorandom number uniformly distributed over $[-0.5, 0.5]$.

The effect of disorder in resonant metasurfaces and photonic crystals has attracted considerable recent interest [58,59]. For highly precise fabrication techniques, such as electron beam lithography, periodicity uncertainties can be minimized to within 1 nm, while standard deviations in unit cell locations and sizes are reduced to approximately 5 nm [9]. Under relatively small disorder conditions ($\sigma_D = 10$ nm), Fig. 10(a) shows that the collective resonance remains robust, although the maximum Purcell and Q factors decrease up to twofold. However, these factors remain an order of magnitude higher than the antibonding resonant modes in Figs. 7 and 9.

Figure 10(b) displays the H_z field distribution, which is antisymmetric with respect to the z axis, for the strongest MQ resonance in the array of identical spheres, labeled MQ_0 in Fig. 10(a). This H_z antisymmetry explains why this odd mode cannot resonate with (or be excited by) a plane wave at normal incidence, as shown in Fig. 10(c). From an electrodynamic perspective, the antisymmetry of the MQ_0 mode arises from interference between the excited multipoles and their driving source, as discussed for the MQ-A mode in Fig. 3. However, a small disorder alters the excited multipoles, breaking the antisymmetry of the H_z field and allowing coupling between the plane wave and the disordered MQ_0 modes, producing resonant peaks such as P_1 in Fig. 10(c). Due to their high-Q resonances, these disordered modes can enhance the trapped magnetic field by up to 250-fold, an order of magnitude greater than the enhancement observed for the antibonding EQ_2 mode in Fig. 9(a).

The inset of Fig. 10(b) shows the far-field distribution of the MQ_0 mode, which does not exhibit radiation along the vertical x axis. In contrast, the MQ-B bonding mode in Fig. 5(d) (the 1D counterpart of MQ_0) demonstrates strong radiation in the x direction. This highlights the importance of considering the collective nature of the entire system when interpreting near- and far-field distributions. A closer examination of the antisymmetry in the MQ_0 mode, shown in Fig. 10(b), reveals that this antisymmetry can be converted into symmetry simply by adding one more row of spheres to form a 9×8 array. This adjustment enables the plane wave to excite a strong collective resonance. In fact, this modification excites the strong resonance labeled P_0 in Fig. 10(d), which also shows the transmittance resulting from the interaction between the bonding resonance and its driving plane wave. Although the coupling remains weak, as indicated by only a 1% change in transmittance across the resonant peak, the near-field enhancement exceeds 250-fold. Figures 10(e) and 10(f) illustrate the symmetry of the components H_z and E_x of the P_0 mode, which are well matched with the normally incident plane wave.

The insets of Figs. 10(e) and 10(f) show the far-field distributions of the transmitted and reflected light, respectively. A strong nonlocal effect is evident in the numerous diffraction orders appearing in both patterns, particularly in transmission. This behavior is promising for applications in the emerging field of nonlocal flat optics.

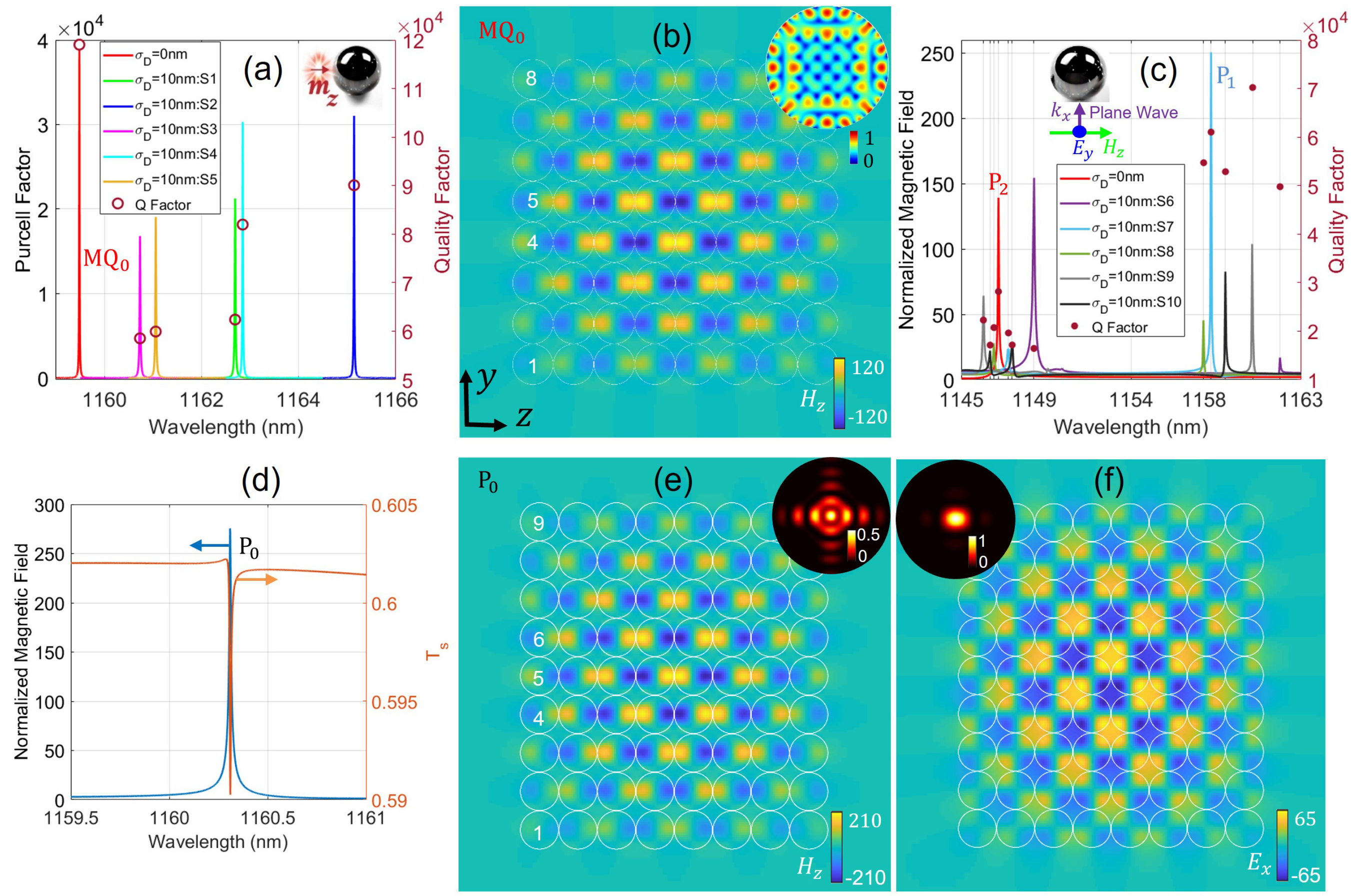

FIG. 10. Dipole and plane-wave excitations of bonding collective resonances and the effects of diameter disorder on coupling. (a) Spectral profiles of the Purcell factor for an in-plane magnetic dipole interacting with the 2D magnetic quadrupole bonding (MQ-B) mode in 8×8 sphere arrays. Two cases are presented: (1) an array of identical spheres ($\sigma_D = 0$ nm) and (2) five arrays with small pseudorandom diameter disorder ($\sigma_D = 10$ nm), labeled S1–S5. The right y axis shows the Q factors of the MQ-B mode for the six samples, revealing that disorder weakens the collective resonances. The inset illustrates the dipole excitation setup. (b) Magnetic field distribution (H_z) for the MQ-B mode in the array of identical spheres [denoted MQ$_0$ in (a)], showing antisymmetry with respect to the z axis. (c) Spectral profiles of the magnetic field for resonant modes excited by a plane wave at normal incidence. The inset shows the plane-wave excitation setup. In an ideal array, the odd MQ$_0$ mode cannot be excited by the plane wave, but disorder introduces coupling between its disordered version (denoted P_1) and the plane wave. (d) Spectral profile of the normalized magnetic field recorded at the center of the 9×8 sphere array, along with the transmittance spectrum, showing only a 1% change across the resonant peak labeled P_0. Both P_0 and MQ$_0$ modes correspond to the band-edge mode for their respective arrays. (e) Magnetic field component (H_z) at the resonant peak in (d), displaying symmetry with respect to the z axis. (f) Electric field component (E_x), showing symmetry with respect to the y axis. Insets in (e) and (f) depict the far-field distributions of light transmitted and reflected from the 9×8 array, respectively.

2. *Effects of increasing disorder on collective resonances*

In the early development of photonic crystals, disorder was believed to play a crucial role in localizing light, drawing inspiration from its effect on localizing electrons via the Anderson mechanism [60]. However, when examining the collective resonances of unit cells, disorder may actually weaken light localization rather than enhance it, as illustrated in Fig. 10(a). To study these effects, we consider increasing levels of disorder in the diameters and positions of the spheres in Fig. 11, which shows the Q factor and peak wavelength of disordered MQ$_0$ modes in 30 arrays. Figures 11(b) and 11(c) and Figs. 11(e) and 11(f) show the magnetic field distributions of four representative samples, labeled MQ$_{1-4}$ in Fig. 11(a).

Increasing the disorder in diameters while keeping the sphere positions fixed, the spectral profiles of the Mie coefficients such as $b_{l'}$ in Eq. (10) fluctuate, while the translational coefficients $A^{l;0}_{l';0}(\overrightarrow{O_u O_n})$ remain unchanged, leading to fluctuations in the resonant wavelength of the collective mode, ranging from approximately 11 nm for $\sigma_D = 20$ nm to around 22 nm for $\sigma_D = 40$ nm. These fluctuations cause some spheres to become off-resonance with others, shifting the collective resonance to a group of spheres where their scattering multipoles resonate most strongly. This is visible in the field distributions shown in Figs. 11(b) and 11(c), where the strongest field locations are not necessarily at the center of the array. In Fig. 11(c), the spheres in the lower-left corner are clearly off-resonant with the rest, acting as scatterers and weakening the collective resonance. The lower number of spheres participating in the collective resonance also contributes to the spectral fluctuation of the resonant peak.

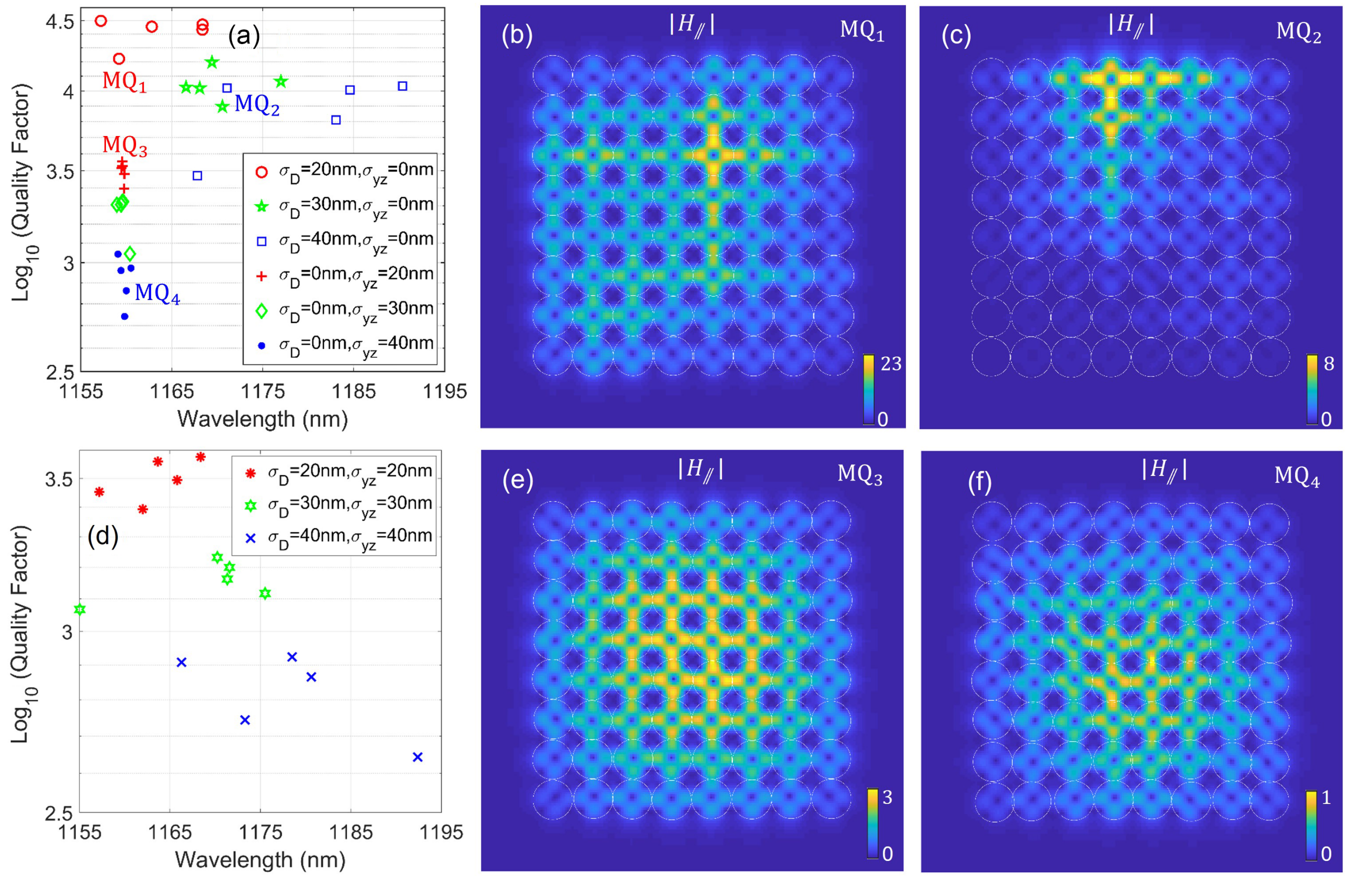

FIG. 11. Effects of increasing disorder in sphere diameter and position on light localization in the 8×8 array. (a) Quality factors and resonant wavelengths of the MQ-B mode in 30 arrays with varying degrees of disorder, either in sphere diameter or position. [(b) and (c)] Magnetic field distributions for two samples, marked in (a), where disorder is introduced only in the sphere diameter, illustrating the robustness of the collective resonances. Despite some spheres being off-resonance, the collective resonance persists, with the maximum field location shifting to the region exhibiting the strongest resonance. (d) Quality factors and resonant wavelengths with strong disorder introduced in both sphere diameter and position. [(e) and (f)] Magnetic field distributions for two modes, indicated in (a), where disorder is introduced only in sphere position, showing that the collective resonance predominantly localizes at the center of the array, in contrast to the distributions seen in (b) and (c).

In contrast, introducing disorder in the in-plane positions of the spheres does not lead to significant spectral fluctuations of the resonant peak. Even with strong positional disorder of $\sigma_{yz} = 40$ nm, allowing fluctuations in both the y and z directions, the resonant peaks across five samples only fluctuate within 2 nm, as shown in Fig. 11(a). However, the Q factor decreases by an order of magnitude compared to the case of diameter disorder alone. This highlights the crucial role of the intersphere distance in maintaining coherent oscillations between scattering multipoles [$A_{l';0}^{l;0}(\overrightarrow{O_u O_n})$ in Eq. (10)]. Positional disorder introduces strong phase fluctuations in the scattering multipoles, leading to lower Q factors. Despite this, since the sphere diameters remain unchanged, their intrinsic modes are preserved, and the trapped light continues to localize near the array center, as shown in Figs. 11(e) and 11(f) for two typical samples.

Figure 11(d) shows the Q factor and peak wavelength with disorder in both the diameters and positions, resulting in characteristics from both types of disorder: The Q factor decreases due to positional disorder, while the wavelength fluctuates widely due to diameter disorder. Nonetheless, even in the most disordered case ($\sigma_D = 40$ nm and $\sigma_{yz} = 40$ nm), the Q factor remains above 440, sufficient for certain nonlinear and lasing applications.

3. *Superiority of bonding modes*

Figure 12 illustrates the prevalence of Bloch bound states below the light line compared to their counterparts above the light line. In finite structures, these Bloch bound states manifest as bonding collective modes, which arise from coupled Mie modes. At subwavelength scales, dominant Mie modes, such as dipole, quadrupole, and octupole, dictate light-matter interactions [4]. When these Mie modes are optically coupled, they typically form bonding photonic bands, as shown in Fig. 12 for the 1D array. Only the MQ resonance is strong enough for its collective resonances to reach the antibonding regime, corresponding to Bloch modes above the light line. Extending this 1D structure into a 2D array reduces radiative losses, enabling Bloch modes from other multipoles, such as the EQ mode, to appear above the light line, as shown in Figs. 8 and 9.

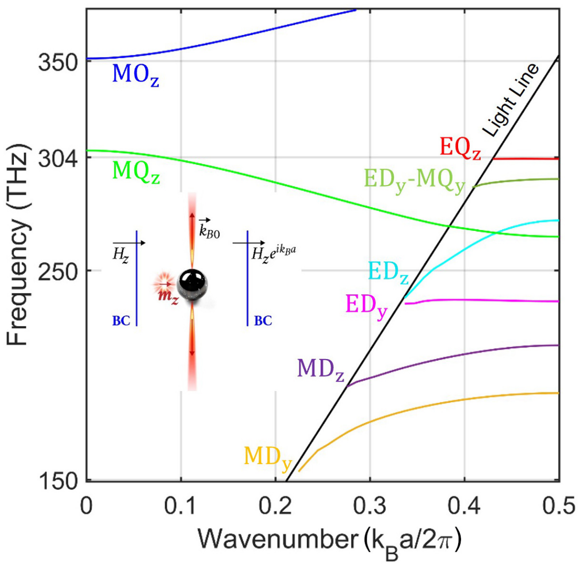

FIG. 12. Prevalence of bonding multipolar modes compared to weaker antibonding counterparts. The inset illustrates the excitation scheme of Bloch waves in a linear array. Due to the axial symmetry of the structure, Bloch modes can be selectively excited by an on-axis magnetic dipole oriented along the y or z axis. These modes form bands primarily originating from a few intrinsic low-order multipoles, including electric dipoles (ED), magnetic dipoles (MD), quadrupoles (EQ, MQ), and octupoles (EO, MO). This work focuses on the MQ_z and MO_z bands excited by a z-oriented magnetic dipole, with particular attention to the infinite Q factors associated with Bloch modes above the light line. Note that the y axis is in frequency units, so the light line appears as a straight line.

In finite structures, bonding collective modes exhibit significantly stronger resonances, with Purcell and Q factors that can be orders of magnitude higher. The strongest resonances are achieved when these collective modes are fine-tuned into their crossing regime, leading to flatband resonances [38]. The ED_y and EQ_z flatbands arising from fine-tuning in Fig. 12 are especially promising for enhancing the Purcell and Q factors.

All photonic modes are subject to radiative losses. Certain antibonding modes, such as the EQ mode shown in Fig. 9, can generate vortex beams when excited by a dipolar emitter, which is promising for nanolaser applications. In terms of far-field distributions, bonding collective modes such as the MQ_0 mode in Fig. 10(b) predominantly emit in-plane, making them particularly advantageous for on-chip nanophotonic circuitry. When focusing on Purcell and Q factors, bonding collective modes are far more promising than their antibonding counterparts.

V. DISCUSSION AND CONCLUSION

A. Near-field and far-field excitation of collective resonances

We present a comprehensive picture of high-Q resonances, encompassing whispering-gallery modes and collective resonances in photonic metastructures. Our focus is on resonant multiple scattering and the multipole expansion of the electromagnetic field, aiming to optimize light-matter interactions. In our Mie-tronics methodology, we consider the 3D environment as a practical continuum. Local excitations using dipoles can excite all available collective resonances, allowing all photonic modes to radiate into the far-field region.

Coupling high-Q resonances with incident free-space beams is inherently complex due to the intricate intrinsic multipolar content of the collective modes. Conventional laser beams may prove inadequate, as their intrinsic modes often do not align favorably with those of the metastructures. Symmetry considerations must account for the collective nature of the resonances rather than focusing solely on field components within a unit cell.

Alternatively, structured light beams with appropriate multipole content could enable efficient coupling between free-space light and collective resonances, particularly for exploring the potential of bonding modes [61,62]. Our proposed Mie-tronics approach not only enhances the development of effective design strategies for high-Q resonances but also offers an alternative to excitation methods based on Bloch waves and group theory [34].

B. Scaling of collective resonances

Our findings offer valuable insights into fundamental limits to Q and Purcell factors within resonant metastructures. In these resonant systems of size N, their Q and Purcell factors follow a power-law scaling $Q(N) \approx N^{\alpha}$. The primary objective in optimizing systems of fixed size N is to maximize α [43]. This scaling parameter is influenced by various properties including the refractive index, unit cell geometry, and dominant Mie modes contributing to collective resonances. We find that generally collective bonding modes exhibit a scaling factor of $\alpha = 3$, at least one polynomial degree higher than their antibonding counterparts. To further increase α, the most promising strategy involves fine-tuning the systems' parameters to merge collective resonances and achieve super-resonances, as exemplified by $\alpha = 6$ in our recent study [38].

Interestingly, the scaling law and fine-tuning effects are also observable in collective responses of field-mediated atoms, each supporting a two-level dipolar transition state [63,64]. The similarity in behavior between atomic and photonic systems arises from the analogy between a resonant mode and a two-level atomic system, as well as the significant role of multiple light scattering in both scenarios [47,65]. Note that while dipole interactions are vital, our photonic systems encompass more general interactions, including higher-order multipole modes, for a comprehensive understanding of collective responses.

C. Similarities and differences between photonic and matter BICs

Our results provide a clear picture of photonic and matter BICs, highlighting both similarities and differences. The original BIC concept revolves around electron localization in potentials that extend infinitely, which supports the BIC as an infinitely narrow resonance [66]. Any introduction of finiteness to these potentials transforms the electronic BIC into a finite-Q resonance [67]. This original BIC is characterized by the divergence of the sum of partial scattering waves [68]. Our understanding of BICs shares two key similarities: our resonant structures also demand infinite extension to induce the divergence of partial multipole waves, and introducing 3D finiteness results in finite-Q resonances.

However, a key distinction exists between our photonic BICs and the original matter-wave BIC. While our photonic BICs remain coupled to a 3D environment, the original matter-wave BIC focused primarily on 1D matter waves. This original BIC relied on layered potential structures, neglecting coupling to higher dimensions and considering only a single continuum channel. The wave confinement mechanism of this BIC was first analyzed by Lord Rayleigh in 1887, predating von Neumann and Wigner's discussions of matter-wave BICs [69], and has been experimentally observed [67]. However, this BIC is peculiar to 1D structures [69]. Such 1D structures are not ideal for interfacing with light emitters, such as quantum dots, because the emitted light can easily couple into propagating waves in other uniform directions. This poor 3D light confinement also applies to structures based on coupled gratings [55] or low-index photonic crystal slabs [22], where multiple light scattering is weak, thus limiting the Purcell enhancement.

The crucial distinction for our photonic BICs, despite their coupling to the 3D environment, lies in the role of retardation effects from Mie resonances. These effects confine light waves temporarily within resonators, enabling strong multiple back-scattering and resulting in the divergence of partial multipole waves at the center of photonic structures. This divergence suggests that achieving high-Q resonances involves maximizing scattering multipole coefficients, leading to the appearance of numerous radiation channels. Interestingly, the oscillating far-field characteristic of our photonic BICs is also a feature of compact matter BICs, such as Friedrich-Wintgen BICs [70,71]. However, the existence of these compact matter BICs relies on closed channels associated with negative energy states—an aspect not applicable to light waves, which inherently have positive energies. Consequently, all light modes function as open channels, precluding the possibility of compact photonic BICs.

D. Collective nature as a unified picture of photonic BICs

Photonic BICs were inspired by the analogy between resonances and closed channels, along with the association of diffraction orders with open channels [33]. Since then, photonic BICs have garnered significant interest within the photonic crystal community, due to their familiarity with Bloch waves and a wide range of potential applications. Much of the research on BICs has focused on diffraction bands above the light line in band diagrams [7,9,22,23]. These studies link BICs to the disappearance of reflectance and transmittance at specific incident angles of plane waves, suggesting complete decoupling from the far-field region [72].

However, our findings challenge this conventional understanding, revealing a paradigm shift: BICs correspond to the divergence of collective resonances that couple to the far field, even in infinitely extended metastructures. Consequently, the widely held belief that BICs collapse in the presence of defects and disorder must be reconsidered [35]. The collective nature of high-Q resonances renders them robust against fabrication defects and structural variations, as the constituent resonators adapt in phase to maintain their collective responses. Moderate structural changes may shift high-Q resonances in spectral space, affecting their strength without destroying them. We have shown that even with a high degree of disorder, characterized by $\sigma_D = 40$ nm and $\sigma_{yz} = 40$ nm, the collective MQ resonance in an array of 8×8 spheres remains sufficiently strong for practical applications.

The collective nature of high-Q resonances explains their robustness, providing an alternative perspective to their commonly associated topological properties [9,23]. Moreover, multipoles inherently possess topological characteristics, offering an explanation for the topological nature of BICs. This reevaluation of the origin of infinite Q factors fundamentally reshapes our understanding of BICs, highlighting the intricate interplay between resonances, scattering, and the far-field region.

In conclusion, the allure of high-Q resonances lies in their capacity to facilitate robust interactions between light and matter. Here we highlighted the potential of collective bonding resonances as a pathway for significantly enhancing interaction efficiency from linear to nonlinear optics and from THz to visible light and beyond.

ACKNOWLEDGMENTS

T.X.H. thanks T. T. H. Do and S.T.Ha for helpful discussions. T.X.H. and Y.K. thank J. Jie and J. Gómez Rivas for helpful discussions. D.L. acknowledges support from the Ministry of Education, Singapore, under its SUTD Kickstarter Initiative (SKI 20210501). Y.K. was supported by the Australian Research Council (Grant No. DP210101292) and the International Technology Center Indo-Pacific (ITC IPAC) via Army Research Office (Contract No. FA520923C0023).

[1] S. Mahmoodian, K. Prindal-Nielsen, I. Söllner, S. Stobbe, and P. Lodahl, Engineering chiral light-matter interaction in photonic crystal waveguides with slow light, Opt. Mater. Express **7**, 43 (2017).

[2] X. Lu, A. McClung, and K. Srinivasan, High-Q slow light and its localization in a photonic crystal microring, Nat. Photon. **16**, 66 (2022).

[3] A. González-Tudela, A. Reiserer, J. J. García-Ripoll, and F. J. García-Vidal, Light–matter interactions in quantum nanophotonic devices, Nat. Rev. Phys. **6**, 166 (2024).

[4] Y. Kivshar, The rise of Mie-tronics, Nano Lett. **22**, 3513 (2022).

[5] K. Shastri and F. Monticone, Nonlocal flat optics, Nat. Photon. **17**, 36 (2023).

[6] C. Schiattarella, S. Romano, L. Sirleto, V. Mocella, I. Rendina, V. Lanzio, F. Riminucci, A. Schwartzberg, S. Cabrini, J. Chen *et al.*, Directive giant upconversion by supercritical bound states in the continuum, Nature (London) **626**, 765 (2024).

[7] C. W. Hsu, B. Zhen, A. D. Stone, J. D. Joannopoulos, and M. Soljačić, Bound states in the continuum, Nat. Rev. Mater. **1**, 16048 (2016).

[8] M. Kang, T. Liu, C. Chan, and M. Xiao, Applications of bound states in the continuum in photonics, Nat. Rev. Phys. **5**, 659 (2023).

[9] J. Jin, X. Yin, L. Ni, M. Soljačić, B. Zhen, and C. Peng, Topologically enabled ultrahigh-Q guided resonances robust to out-of-plane scattering, Nature (London) **574**, 501 (2019).

[10] J. D. Joannopoulos, S. G. Johnson, J. N. Winn, and R. D. Meade, *Photonic Crystals: Molding the Flow of Light* (Princeton University Press, Princeton, NJ, 2008).

[11] M.-S. Hwang, H.-C. Lee, K.-H. Kim, K.-Y. Jeong, S.-H. Kwon, K. Koshelev, Y. Kivshar, and H.-G. Park, Ultralow-threshold laser using super-bound states in the continuum, Nat. Commun. **12**, 4135 (2021).

[12] Z. Chen, X. Yin, J. Jin, Z. Zheng, Z. Zhang, F. Wang, L. He, B. Zhen, and C. Peng, Observation of miniaturized bound states in the continuum with ultra-high quality factors, Sci. Bull. **67**, 359 (2022).

[13] L. Wu, H. Wang, Q. Yang, Q.-X. Ji, B. Shen, C. Bao, M. Gao, and K. Vahala, Greater than one billion Q factor for on-chip microresonators, Opt. Lett. **45**, 5129 (2020).

[14] T. X. Hoang, H.-S. Chu, F. J. García-Vidal, and C. E. Png, High-performance dielectric nano-cavities for near-and mid-infrared frequency applications, J. Opt. **24**, 094006 (2022).

[15] C. Couteau, S. Barz, T. Durt, T. Gerrits, J. Huwer, R. Prevedel, J. Rarity, A. Shields, and G. Weihs, Applications of single photons to quantum communication and computing, Nat. Rev. Phys. **5**, 326 (2023).

[16] A. Kodigala, T. Lepetit, Q. Gu, B. Bahari, Y. Fainman, and B. Kanté, Lasing action from photonic bound states in continuum, Nature (London) **541**, 196 (2017).

[17] S. T. Ha, Y. H. Fu, N. K. Emani, Z. Pan, R. M. Bakker, R. Paniagua-Domínguez, and A. I. Kuznetsov, Directional lasing in resonant semiconductor nanoantenna arrays, Nat. Nanotechnol. **13**, 1042 (2018).

[18] Z. Liu, Y. Xu, Y. Lin, J. Xiang, T. Feng, Q. Cao, J. Li, S. Lan, and J. Liu, High-Q quasibound states in the continuum for nonlinear metasurfaces, Phys. Rev. Lett. **123**, 253901 (2019).

[19] S. G. Johnson, S. Fan, P. R. Villeneuve, J. D. Joannopoulos, and L. A. Kolodziejski, Guided modes in photonic crystal slabs, Phys. Rev. B **60**, 5751 (1999).

[20] S. Fan and J. D. Joannopoulos, Analysis of guided resonances in photonic crystal slabs, Phys. Rev. B **65**, 235112 (2002).

[21] J. Y. Vaishnav, J. D. Walls, M. Apratim, and E. J. Heller, Matter-wave scattering and guiding by atomic arrays, Phys. Rev. A **76**, 013620 (2007).

[22] C. W. Hsu, B. Zhen, J. Lee, S.-L. Chua, S. G. Johnson, J. D. Joannopoulos, and M. Soljačić, Observation of trapped light within the radiation continuum, Nature (London) **499**, 188 (2013).

[23] B. Zhen, C. W. Hsu, L. Lu, A. D. Stone, and M. Soljačić, Topological nature of optical bound states in the continuum, Phys. Rev. Lett. **113**, 257401 (2014).

[24] E. N. Bulgakov and D. N. Maksimov, Topological bound states in the continuum in arrays of dielectric spheres, Phys. Rev. Lett. **118**, 267401 (2017).

[25] K. Sun, W. Wang, and Z. Han, High-Q resonances in periodic photonic structures, Phys. Rev. B **109**, 085426 (2024).

[26] A. Devaney and E. Wolf, Multipole expansions and plane wave representations of the electromagnetic field, J. Math. Phys. **15**, 234 (1974).

[27] T. X. Hoang, X. Chen, and C. J. Sheppard, Multipole and plane wave expansions of diverging and converging fields, Opt. Express **22**, 8949 (2014).

[28] R. Richtmyer, Dielectric resonators, J. Appl. Phys. **10**, 391 (1939).

[29] T. X. Hoang, S. N. Nagelberg, M. Kolle, and G. Barbastathis, Fano resonances from coupled whispering–gallery modes in photonic molecules, Opt. Express **25**, 13125 (2017).

[30] T. X. Hoang, X. Chen, and C. J. R. Sheppard, Interpretation of the scattering mechanism for particles in a focused beam, Phys. Rev. A **86**, 033817 (2012).

[31] M. S. Sidorenko, O. N. Sergaeva, Z. F. Sadrieva, C. Roques-Carmes, P. S. Muraev, D. N. Maksimov, and A. A. Bogdanov, Observation of an accidental bound state in the continuum in a chain of dielectric disks, Phys. Rev. Appl. **15**, 034041 (2021).

[32] Z. Sadrieva, K. Frizyuk, M. Petrov, Y. Kivshar, and A. Bogdanov, Multipolar origin of bound states in the continuum, Phys. Rev. B **100**, 115303 (2019).

[33] D. C. Marinica, A. G. Borisov, and S. V. Shabanov, Bound states in the continuum in photonics, Phys. Rev. Lett. **100**, 183902 (2008).

[34] A. C. Overvig, S. C. Malek, M. J. Carter, S. Shrestha, and N. Yu, Selection rules for quasibound states in the continuum, Phys. Rev. B **102**, 035434 (2020).

[35] G. Xu, H. Xing, Z. Xue, D. Lu, J. Fan, J. Fan, P. P. Shum, and L. Cong, Recent advances and perspective of photonic bound states in the continuum, Ultrafast Sci. **3**, 0033 (2023).

[36] J. Lee, B. Zhen, S.-L. Chua, W. Qiu, J. D. Joannopoulos, M. Soljačić, and O. Shapira, Observation and differentiation of unique high-Q optical resonances near zero wave vector in macroscopic photonic crystal slabs, Phys. Rev. Lett. **109**, 067401 (2012).

[37] T. X. Hoang, S. T. Ha, Z. Pan, W. K. Phua, R. Paniagua-Domínguez, C. E. Png, H.-S. Chu, and A. I. Kuznetsov, Collective Mie resonances for directional on-chip nanolasers, Nano Lett. **20**, 5655 (2020).

[38] T. X. Hoang, D. Leykam, and Y. Kivshar, Photonic flatband resonances in multiple light scattering, Phys. Rev. Lett. **132**, 043803 (2024).

[39] M. J. Hartmann, F. G. Brandao, and M. B. Plenio, Strongly interacting polaritons in coupled arrays of cavities, Nat. Phys. **2**, 849 (2006).

[40] A. Reiserer and G. Rempe, Cavity-based quantum networks with single atoms and optical photons, Rev. Mod. Phys. **87**, 1379 (2015).

[41] D. E. Chang, J. S. Douglas, A. González-Tudela, C.-L. Hung, and H. J. Kimble, *Colloquium:* Quantum matter built from nanoscopic lattices of atoms and photons, Rev. Mod. Phys. **90**, 031002 (2018).

[42] N. Ustimenko, C. Rockstuhl, and A. B. Evlyukhin, Resonances in finite-size all-dielectric metasurfaces for light trapping and propagation control, Phys. Rev. B **109**, 115436 (2024).

[43] M. Mikhailovskii, M. Poleva, N. Solodovchenko, M. Sidorenko, Z. Sadrieva, M. Petrov, A. Bogdanov, and R. Savelev, Engineering of high-Q states via collective mode coupling in chains of Mie resonators, ACS Photon. **11**, 1657 (2024).

[44] Y. E. Geints, Phase-controlled supermodes in symmetric photonic molecules, J. Quant. Spectrosc. Radiat. Transf. **302**, 108524 (2023).
[45] Y. E. Geints, Manipulating the supermodes in photonic molecules: Prospects for all-optical switching and sensing, J. Opt. Soc. Am. B **40**, 1875 (2023).
[46] E. N. Bulgakov and A. F. Sadreev, High-Q resonant modes in a finite array of dielectric particles, Phys. Rev. A **99**, 033851 (2019).
[47] A. Lagendijk and B. A. Van Tiggelen, Resonant multiple scattering of light, Phys. Rep. **270**, 143 (1996).
[48] K. Koshelev, Y. Kivshar, and A. Bogdanov, Engineering with bound states in the continuum, Opt. Photon. News **31**, 38 (2020).
[49] V. Giannini, G. Vecchi, and J. Gómez Rivas, Lighting up multipolar surface plasmon polaritons by collective resonances in arrays of nanoantennas, Phys. Rev. Lett. **105**, 266801 (2010).
[50] A. D. Utyushev, V. I. Zakomirnyi, and I. L. Rasskazov, Collective lattice resonances: Plasmonics and beyond, Rev. Phys. **6**, 100051 (2021).
[51] J. B. Khurgin and G. Sun, Comparative analysis of spasers, vertical-cavity surface-emitting lasers and surface-plasmon-emitting diodes, Nat. Photon. **8**, 468 (2014).
[52] S. Rodriguez, M. Schaafsma, A. Berrier, and J. G. Rivas, Collective resonances in plasmonic crystals: Size matters, Phys. B: Condens. Matter **407**, 4081 (2012).
[53] C. J. Chang-Hasnain and W. Yang, High-contrast gratings for integrated optoelectronics, Adv. Opt. Photon. **4**, 379 (2012).
[54] V. Ardizzone, F. Riminucci, S. Zanotti, A. Gianfrate, M. Efthymiou-Tsironi, D. Suàrez-Forero, F. Todisco, M. De Giorgi, D. Trypogeorgos, G. Gigli *et al.*, Polariton Bose–Einstein condensate from a bound state in the continuum, Nature (London) **605**, 447 (2022).
[55] N. D. Le, P. Bouteyre, A. Kheir-Aldine, F. Dubois, S. Cueff, L. Berguiga, X. Letartre, P. Viktorovitch, T. Benyattou, and H. S. Nguyen, Super bound states in the continuum on a photonic flatband: Concept, experimental realization, and optical trapping demonstration, Phys. Rev. Lett. **132**, 173802 (2024).
[56] Y. Zhou, M. Moewe, J. Kern, M. C. Huang, and C. J. Chang-Hasnain, Surface-normal emission of a high-Q resonator using a subwavelength high-contrast grating, Opt. Express **16**, 17282 (2008).
[57] X. Jia, J. Kapraun, J. Wang, J. Qi, Y. Ji, and C. Chang-Hasnain, Metasurface reflector enables room-temperature circularly polarized emission from vcsel, Optica **10**, 1093 (2023).
[58] C. Liu, M. V. Rybin, P. Mao, S. Zhang, and Y. Kivshar, Disorder-immune photonics based on Mie-resonant dielectric metamaterials, Phys. Rev. Lett. **123**, 163901 (2019).
[59] Z. Hu, C. Liu, and G. Li, Disordered optical metasurfaces: From light manipulation to energy harvesting, Adv. Phys.: X **8**, 2234136 (2023).
[60] S. John, Strong localization of photons in certain disordered dielectric superlattices, Phys. Rev. Lett. **58**, 2486 (1987).
[61] T. X. Hoang, X. Chen, and C. J. Sheppard, Multipole theory for tight focusing of polarized light, including radially polarized and other special cases, J. Opt. Soc. Am. A **29**, 32 (2012).
[62] K. Y. Bliokh, E. Karimi, M. J. Padgett, M. A. Alonso, M. R. Dennis, A. Dudley, A. Forbes, S. Zahedpour, S. W. Hancock, H. M. Milchberg *et al.*, Roadmap on structured waves, J. Opt. **25**, 103001 (2023).
[63] Y.-X. Zhang and K. Mølmer, Subradiant emission from regular atomic arrays: Universal scaling of decay rates from the generalized Bloch theorem, Phys. Rev. Lett. **125**, 253601 (2020).
[64] I. A. Volkov, N. A. Ustimenko, D. F. Kornovan, A. S. Sheremet, R. S. Savelev, and M. I. Petrov, Strongly subradiant states in planar atomic arrays, Nanophotonics **13**, 289 (2024).
[65] S. Asselie, A. Cipris, and W. Guerin, Optical interpretation of linear-optics superradiance and subradiance, Phys. Rev. A **106**, 063712 (2022).
[66] F. H. Stillinger and D. R. Herrick, Bound states in the continuum, Phys. Rev. A **11**, 446 (1975).
[67] F. Capasso, C. Sirtori, J. Faist, D. L. Sivco, S.-N. G. Chu, and A. Y. Cho, Observation of an electronic bound state above a potential well, Nature (London) **358**, 565 (1992).
[68] F. Stillinger, Potentials supporting positive-energy eigenstates and their application to semiconductor heterostructures, Physica B+C **85**, 270 (1976).
[69] E. Yablonovitch, Photonic crystals: What's in a name? Opt. Photon. News **18**, 12 (2007).
[70] L. Fonda, Bound states embedded in the continuum and the formal theory of scattering, Ann. Phys. **22**, 123 (1963).
[71] H. Friedrich and D. Wintgen, Interfering resonances and bound states in the continuum, Phys. Rev. A **32**, 3231 (1985).
[72] Z. Dong, Z. Mahfoud, R. Paniagua-Domínguez, H. Wang, A. I. Fernández-Domínguez, S. Gorelik, S. T. Ha, F. Tjiptoharsono, A. I. Kuznetsov, M. Bosman *et al.*, Nanoscale mapping of optically inaccessible bound-states-in-the-continuum, Light Sci. Appl. **11**, 20 (2022).